Two-dimensional Navier–Stokes simulation of breaking waves

Gang Chen, Christian Kharif, Stéphane Zaleski, Jie Li

Two-dimensional Navier–Stokes simulation of breaking waves

Gang Chen and Christian Kharif

Institut de Recherche sur les Phénomènes Hors Equilibre, UMR CNRS 6594, Case 903, 163, avenue de Luminy, 13288 Marseille Cedex 9, France

Stéphane Zaleski and Jie Li

Laboratoire de Modélisation en Mécanique, URA CNRS 229, Université Pierre et Marie Curie, 4 place Jussieu, 75252 Paris Cedex 05, France

Abstract

Numerical simulations describing plunging breakers including the splash-up phenomenon are presented. The motion is governed by the classical, incompressible, two-dimensional Navier-Stokes equation. The numerical modelling of this two-phase flow is based on a piecewise linear version of the volume of fluid method. Capillary effects are taken into account such as a nonisotropic stress tensor concentrated near the interface. Results concerning the time evolution of liquid–gas interface and velocity field are given for short waves, showing how an initial steep wave undergoes breaking and successive splash-up cycles. Breaking processes including overturning, splash-up and gas entrainment, and breaking induced vortex-like motion beneath the surface and energy dissipation, are presented and discussed. It is found that strong vorticities are generated during the breaking process, and that more than 80% of the total pre-breaking wave energy is dissipated within three wave periods. The numerical results are compared with some laboratory measurements, and a favorable agreement is found.

Revised manuscript **PF# 3885A**

1. INTRODUCTION

The breaking of surface waves in deep water has received considerable attention over the last two decades because of both fundamental interest and its implications in oceanography and naval hydrodynamics. For example, it is well known that breaking waves play an important role in the air-sea interaction such as the transfer of heat, momentum and mass between the atmosphere and ocean; the production of spray, aerosols and bubbles, and the generation of turbulence in the sea (for a recent review see Melville[1]). Breaking waves exert by far the largest wave-induced force (often in the form of impacts) on offshore structures and ships in heavy seas, which may cause serious safety problems and structure damage of the systems. Hence, it is of great importance to understand the mechanics of breaking process.

However, the breaking process is difficult to measure and to model owing to its physical complexities involved. The breaking is a highly nonlinear phenomenon involving two-phase and turbulent flow, and the process is intermittent in space and time. In view of these difficulties, our current understanding of breaking process, in particular the later stage of breaking is based in large part on the well-controlled laboratory experimental investigations. Two modes, e.g. quasi-stationary and propagating, have been used to study respectively the spilling[2,3] and plunging breakers.[4,5] Good description of basic properties of unsteady deep-water breaking waves, such as the geometric properties, the phenomenon of splash-up, the mode of air entrainment, was reported by Bonmarin.[4] The most comprehensive laboratory studies have been made by Rapp and Melville.[5] They measured surface motion, momentum and energy fluxes, breaking induced-current and turbulence, surface mixing, and energy dissipation.

Numerical simulation of the evolution of breaking wave was first performed by Longuet-Higgins and Cokelet[6] using boundary integral method (based on potential flow). Since then a number of more robust, accurate and efficient numerical codes have been developed successfully to describe the evolution of two-dimensional surface wave up to breaking, but they are unable to continue beyond the point at which the surface impacts on itself (see for more detailed reviews Peregrine,[9] and Banner and Peregrine[10]). Numerical computations suggest that the local particle velocity in a plunging breaker can have almost twice the

linear phase speed, and that the acceleration of particles in the free surface can have up to six times that of gravity. The validity and usefulness of potential-flow computations for predicting overturning waves up to breaking were examined and confirmed by several independent comparisons of surface profile and velocity field in a deep-water breaking wave to the experimental measurements (see for example Dommermuth *et al.*[11] and Skyner[12]). More recently, by using particle image velocimetry (PIV) and particle tracking velocimetry (PTV) techniques, Perlin *et al.*[13] obtained full-field velocity in a deep-water plunging breaker. Their vorticity calculations based on the measured velocity fields further confirm that the flows are almost irrotational up to the impact of jet onto the forward face of the water surface, and that plunging breaking has an insignificant influence on particle motions at depths greater than half the wavelength.

There is little numerical simulation of this problem going beyond the time of impact of the plunging jet. In Monaghan *et al.*,[14] the smoothed particle hydrodynamics method (SPH) was used to simulate the phenomenon of splash-up. However only one figure showing splash-up was given and the spatial resolution of the method seems insufficient to resolve the small scale viscous and capillary effects. The aim of the present work is to attempt a numerical solution of the *Navier–Stokes equations* of this problem, on grids sufficiently fine so that viscous and capillary effects could be retained. We wish to simulate the *two-phase flow* of bubbles and droplets following splash-up as well as vortex-like motions, and to investigate the role of breaking on the generation of vorticity and on the dissipation of wave energy. To this end, we have used a robust numerical technique, based on the volume of fluid method[15–22] that allows us to use rather large grids and to follow large interface deformations and topology changes during the breaking process.

In Sec. II, we present the global formulation for two-fluid flows and the numerical methods used in this work. Sec. III reports on a series of numerical experiments, including simulations of capillary waves and interfacial gravity waves, to illustrate the accuracy of the numerical code. The initial condition used to obtain a breaking wave and parameters of computations are given in Sec. IV. Numerical results are presented and discussed in Sec. V. These include jet formation, phenomenon of splash-up, gas entrainment, breaking induced

vortex-like motion beneath the surface and energy dissipation during the breaking process. Computations are compared with some laboratory measurements. Summary and concluding remarks are presented in Sec. VI.

2. FORMULATION AND NUMERICAL METHOD

A. Global formulation for two-fluid flows

We consider the incompressible flow of two immiscible fluids. For convenience in what follows, we shall call one of the fluids a liquid and the other a gas (see Fig.1). The mathematical idealization of the problem is that of a two-dimensional flow with a constant surface tension σ on the liquid-gas interface and viscous dissipation in the bulk. Let δ_S be a delta function concentrated on the surface S, then the governing equations for the velocity vector $\mathbf{u} = (u, v)$ and pressure p in the bulk of each phase (liquid and gas) are the classical Navier-Stokes equations supplemented by the condition of incompressibility:

$$\rho\left(\frac{\partial \mathbf{u}}{\partial t} + \mathbf{u}\cdot\nabla\,\mathbf{u}\right) = -\nabla p + \nabla\cdot(2\mu\mathbf{D}) + \rho\mathbf{g} + \sigma\kappa\delta_S\mathbf{n}, \tag{1}$$

$$\nabla\cdot\mathbf{u} = 0, \tag{2}$$

where ρ is the density and μ is the dynamical viscosity. They are constant in each phase but may exhibit large jumps across phase boundaries. $\mathbf{D}$ is the rate of deformation tensor whose components are $D_{ij} = (\partial u_i/\partial x_j + \partial u_j/\partial u_i)/2$, and $\mathbf{g} = (0, -g)$ is the acceleration due to gravity. The term $\sigma\kappa\delta_S\mathbf{n}$ represents capillary forces, with $\mathbf{n}$ the unit normal to the interface. The curvature of the interface is κ and may be expressed as

$$\kappa = -\nabla_S\cdot\mathbf{n}, \tag{3}$$

where ∇_S is the gradient operator restricted to the surface S.

It is possible to rewrite the Navier-Stokes equations in an explicit momentum conserving form. In particular, capillary effects may be represented by a capillary pressure tensor, denoted $\mathbf{T}$. This tensor is tangent to the interface and given by

$$\mathbf{T} = -\sigma(\mathbf{I} - \mathbf{n} \otimes \mathbf{n})\delta_S, \tag{4}$$

where $\mathbf{I}$ is the unit tensor δ_{ij}. Furthermore, it is shown (see Lafaurie *et al.*[21]) that the capillary force may be written in the form

$$\sigma\kappa\delta_S\mathbf{n} = -\nabla \cdot \mathbf{T}. \tag{5}$$

One then obtains the following equivalent formulation to equation (1)

$$\frac{\partial(\rho\mathbf{u})}{\partial t} = -\nabla \cdot (p\mathbf{I} + \rho\mathbf{u} \otimes \mathbf{u} - 2\mu\mathbf{D} + \mathbf{T}) + \rho\mathbf{g}. \tag{6}$$

Apart from its momentum conserving nature, this representation of surface tension stresses is especially interesting for the simulation of wave breaking, since it avoids the singularity which would occur in the continuum limit when interfaces change topology and the curvature becomes locally infinite.

The numerical solution of the basic equations is based on the method described in Lafaurie *et al.*[21] Briefly, the Navier-Stokes equations (6) are solved using finite differences on a staggered (MAC) Eulerian grid and split-explicit time differencing scheme. The incompressibility condition (2) is accurately satisfied by a projection method[23] with the help of a multigrid Poisson solver.[24] This yields, at each time step, a velocity field $\mathbf{u}$ which is used to propagate the interface by a volume of fluid type numerical technique as described below. This method allows us to follow interfaces beyond the point of reconnection, and is relatively simple and robust.

B. Interface reconstruction and evolution

The existing methods for the treatment of interfaces between immiscible fluids can be divided into two broad categories (see, for example, Floryan and Rasmussen[18]): interface tracking and interface capturing. In interface tracking methods the interface is specified by a series of interpolated curves through a discrete set of marker points located on the interface. Although this method can follow the evolution of a simple interface very accurately, its implementation poses difficulties in dealing with changes in interface topology. In interface capturing methods a data structure is defined in the entire computational domain, say, volume fractional field,

C. The interface is captured in the sense that the actual physical discontinuity is someplace near the middle of the gradient. This method is capable of handing merging and folding interfaces and is relatively simple to implement. Volume of fluid (VOF) methods[15–22] fall in this category and have been widely used in the numerical simulation of viscous flows with moving interfaces. In this method, one divides the computational domain into a number of computational cells (i, j), the representation of the interface is made with the help of the volume fraction C_{ij} in cell (i, j). The field $C_{i,j}$, with $C = 1$ inside one fluid (liquid for example) and $C = 0$ in the other, is also called the color function. The interfaces occur in cells with fractional volumes, i.e. $0 < C_{ij} < 1$. In the interface cells, the density and viscosity in equation (6) are linearly interpolated between two phases

$$\rho = C\rho_L + (1 - C)\rho_G, \tag{7}$$

$$\mu = C\mu_L + (1 - C)\mu_G, \tag{8}$$

where the subscripts L and G denote respectively the liquid and gas phases.

Reconstructing the interface from the field C_{ij} is the first task in the VOF method. An ideal representation of the interface would be a series of exactly matching segments, i.e. segments connecting the sides of the cells, but this increases the computational complexity and in practice is difficult to realize because it is necessary to solve a coupled system of algebraic equations at each time step. In this work, the so-called Piecewise Linear Interface Construction or PLIC method[22] is used. The exact matching is abandoned, but the algorithm is faster and relatively simple.

PLIC method involves the following three steps. First, the interface is approximated by a segment in each (interface) cell independently. The normal of the segment is estimated using finite-difference approximations based on the neighboring cells. Once the normal is computed one adjusts the position of the segment to obtain a volume fraction equal to the prescribed value C_{ij}. In a second step, the interface motion is computed in a Lagrangian manner with velocities obtained by linear interpolation. Finally, the volume fractions are recalculated. With the PLIC method, the position of the interface is reconstructed with errors of order $O(\kappa h^2)$, where κ is the local curvature of the interface and h is the mesh size,

and thus more accurately than in most volume of fluid methods, including that of Lafaurie *et al.*[21] Indeed, during the simulations, we observe that only a very small fraction of mass is lost. For instance, in the complex case of Fig.4 this fraction is less that $1.2 \times 10^{-3}\%$ over the entire simulation.

All the computations described herein are carried out in a square box. The motion is assumed to be periodic in the horizontal coordinate x, though not necessarily in the time t. In order to simulate the wave kinematics and dynamics in infinite depth, we have used the free-slip condition at the bottom and top boundaries. Note that no-slip condition has also been used at the bottom and top boundaries, but no difference in numerical results was observed. This confirms in fact that breaking has no influence on the particle motion at depths greater than half the wavelength.[13]

3. CODE VERIFICATION

The verification of the validity of the numerical code was made through a series of numerical experiments. As a first test, we performed the simulation of pure capillary waves ($\mathbf{g} = 0$) propagating on the interface between two viscous fluids in a square box of length equal to the wavelength λ. Taking as a length scale λ and as a time scale $(\rho_L \lambda^3/\sigma)^{1/2}$, the problem is then defined by three dimensionless parameters: the density ratio $\overline{\rho} = \rho_G/\rho_L$, the viscosity ratio $\overline{\mu} = \mu_G/\mu_L$ and the Ohnesorge number $Oh = \mu_L/(\sigma\rho_L\lambda)^{1/2}$ (For a characteristic length ℓ the Ohnesorge number is defined as $Oh = (\ell_\mu/\ell)^{1/2}$, where ℓ_μ is the viscous capillary length which is defined for a fluid of viscosity μ and density ρ by $\ell_\mu = \mu^2/(\rho\sigma)$).

The initial conditions correspond to a linear cosine capillary wave. We carried out computations for $\overline{\rho} = 0.01$, $\overline{\mu} = 0.1$ and $Oh = 0.01$, and compared the measured frequency Ω_N with the theoretical prediction for small-amplitude capillary waves (Lamb,[25] §266):

$$\Omega = \frac{(2\pi)^{3/2}}{(1+\overline{\rho})^{1/2}}\,. \tag{9}$$

The amplitude of the wave was decreased until no variation in the measured frequency was seen. The ratio Ω_N/Ω is plotted in Fig.2(a) versus mesh size h. It can be seen that the computation converged to a value of the frequency which, however, is not exactly the

theoretical predicted one, but the difference is within 3%. This (small) discrepancy can be explained by the fact that there is a very small viscous contribution to the frequency in a typical computation of viscous capillary waves, and such effect, however, is not accounted for in the dispersion relation (9). The numerical diffusion due to discretization may also attribute to this discrepancy.

In Fig.2(b), we display the evolution of interface position at $x = 0$ and compare it with the expected decay rate γ due to viscous effects:

$$\gamma = 8\pi^2 \frac{1+\overline{\mu}}{1+\overline{\rho}} Oh + 2\pi Oh^{1/2} \frac{(2\Omega \overline{\rho}\,\overline{\mu})^{1/2}}{(1+\overline{\rho})\,(1+(\overline{\rho}\,\overline{\mu})^{1/2})}\,. \tag{10}$$

It is seen that the decay in time of the capillary wave was reproduced by the numerical simulation.

To further test aspects of the algorithm and to illustrate the accuracy of the numerical code, we performed a series of simulations of gravity waves propagating on the interface between two viscous fluids. Taking as a length scale the wavelength λ and a characteristic time $(\lambda/g)^{1/2}$ of the wave, the problem has four dimensionless parameters. They are the (liquid) Reynolds number $Re = \rho_L g^{1/2} \lambda^{3/2}/\mu_L$, the Bond number $B = \rho_L g \lambda^2/\sigma$, the density ratio $\overline{\rho} = \rho_G/\rho_L$ and the viscosity ratio $\overline{\mu} = \mu_G/\mu_L$. The results of our computation for $Re = 10^3$, $B = 10^3$, $\overline{\rho} = 0.01$ and $\overline{\mu} = 0.1$ are shown in Fig.3 where we plot the evolution of interface position at $x = 0$ and compare it with the theoretical prediction of the decay rate γ for small-amplitude gravity waves:

$$\gamma = 8\pi^2 \frac{1+\overline{\mu}}{1+\overline{\rho}} Re^{-1} + 2\pi Re^{-1/2} \frac{(2\Omega \overline{\rho}\,\overline{\mu})^{1/2}}{(1+\overline{\rho})\,(1+(\overline{\rho}\,\overline{\mu})^{1/2})}\,, \tag{11}$$

with the frequency Ω given by the dispersion relation (Lamb,[25] §267)

$$\Omega = \left(2\pi \frac{1-\overline{\rho}}{1+\overline{\rho}} + 8\pi^3 B^{-1} \frac{1}{1+\overline{\rho}} \right)^{1/2}\,. \tag{12}$$

The initial conditions of the computation were linear cosine gravity interfacial waves. As Fig.(3) makes clear, the decay in time of a sufficient small-amplitude gravity wave was well reproduced by the numerical computation. With a grid size of 128×128, the measured frequency is 2.534 and it is 2.533 with 256×256 resolution which agrees with the expected linearized frequency ($\Omega = 2.531$) to within 1%.

In summary, these computations and favorable comparisons provide a strong validation of the numerical results reported below .

4. CONDITION OF COMPUTATION

In this section, we present the initial condition used to generate a breaking wave. It is known[5] that wave breaking in the field may result from direct wind forcing, wave-wave interaction or wave instability. Numerical computations of breaking waves usually form waves by applying a pressure forcing at the surface[6,28] or obtain breaking conditions simply from an unsteady wave having a large enough amplitude.[27,29] Note that the nonlinear development of the lowest superharmonic instability of a steep Stokes wave may also lead to wave breaking.[7,8] We present here the results for waves developing from the initial condition that corresponds to a Stokes wave in infinite depth calculated at the third order of wave amplitude a.

Let x and y denote respectively the horizontal and vertical coordinates, and the origin be taken in the center of the box (see Fig.1), then using the same reference scales as in the previous case of gravity waves, the initial wave profile ($t = 0$), η, of slope ϵ ($= 2\pi a/\lambda$) is (see, for example, Lamb,[25] §250)

$$\eta(x,0) = \frac{1}{2\pi}\left(\epsilon\cos(2\pi x) + \frac{1}{2}\epsilon^2\cos(4\pi x) + \frac{3}{8}\epsilon^3\cos(6\pi x)\right). \tag{13}$$

The initial wave slope ϵ was set to be 0.55. Since it is not a steadily traveling wave and is steeper than any irrotational steady wave, such initial conditions evolve to breaking as shown below. Although we obtain quantitative information for several breaking intensities as determined by the initial wave slope ϵ, we focus, in this paper, only on the plunging breaker which is the most powerful breaker in deep and shallow water, and which is believed to play an important role in air–sea interactions, especially for mass transfer phenomena across the water surface. We present numerical results for $Re = 10^4$, $\overline{\rho} = 10^{-2}$, $\overline{\mu} = 0.4$ and $B = 10^4$, as other plunging breakers give qualitatively similar results. Computations were performed on comparatively large grids, i.e. 512×512 uniform mesh, with a constant time step of 10^{-4}.

Before presenting numerical results it is useful to make some comments on the physical scales that we are trying to simulate. There are two dimensionless numbers which are related

to the length scale (i.e. the wavelength λ): the Reynolds number Re and the Bond number B. Based on these two numbers and for a given liquid, one then obtains two (different) length scales, say ℓ_{Re} and ℓ_B respectively. Specifically, if it were water and for $Re = 10^4$ and $B = 10^4$, the physical scales would be $\ell_{Re} \approx 2.5cm$ and $\ell_B \approx 27cm$. We did not use real physical properties of air and water in the computations because of the limitations in the range of dimensionless numbers. It is well known that when the Reynolds number becomes too large, one expects the formation of boundary layers smaller than the mesh size, thus a loss of accuracy. In practice we reach without trouble Reynolds numbers of order 10^4 (in the liquid phase) for boxes of size 512×512. At small Bond number, surface tension dominates the inertial phenomena and one observes easily periodic capillary waves. This is one of reasons why first order VOF methods, such as the SOLA-VOF method[15] are numerically instable in the absence of surface tension. The interface is progressively destroyed by the generation of floatsam and surface tension is the only way to keep the interface stable. On the other hand, the PLIC method[22] that we used avoids the numerical instability. The small structures created at large Bond number have a more physical meaning. Therefore, the values of the dimensionless numbers have been chosen so as to reach the compromise between the accuracy of computations and the physical phenomena which we are interested in. In other words, we are trying to simulate dynamics of short gravity breaking waves. At these physically relevant scales, the flow under breaking waves is believed not to be fully developed turbulent, instead, it is in a laminar-turbulent transition. On the other hand, we solved directly the full Navier-Stokes equations which are appropriate to the physical phenomena at this Reynolds number. It is highly interesting to incorporate an adequate turbulence model into the present numerical scheme. A full discussion of this question is beyond the scope of the present paper, except to remark that most of existing numerical models for breaking waves, e.g. based on depth-integrated equations, mixing length models or simplified turbulent kinetic energy $k-$equation, can not describe the wave breaking process adequately, because these "rudimentary" turbulence models are unable to trait the situation far from equilibrium such as the wave breaking process. It is also difficulty to determine a proper length scale of the turbulence in the breaking zone. In the future, we will examine

the manner in which different turbulent models (e.g. $k-\epsilon$ and Reynolds Stress models) can be incorporated within the present numerical technique.

5. RESULTS AND DISCUSSION

A. General description of the breaking process

Figure 4 shows snapshots of a time series of the wave evolution and breaking process up to time $t = 8$ (noting that the present length and time scales are chosen such that a linear cosine wave has a period of $(2\pi)^{1/2}$). The initial wave given by (13) has its crest at $x = 0$ and is moving from left to right. At $t = 0$, the velocity field in the liquid part is obtained from the velocity potential (without surface tension, i.e. $B \to \infty$), while the gas is at rest, and then motion is generated in the bulk of the gas phase through dynamical coupling with liquid at the interface. As a periodic boundary condition is imposed in the direction of wave propagation, the fluid moving out of the domain on the right will rejoin it on the left. It is seen that the wave breaks in the form of plunging. During the pre-breaking stage, the wave profile, particularly near the crest, becomes more and more asymmetric (Fig.4(a)), while the trough remains relatively smooth. The wave breaks at the time when the front face of the crest steepens and becomes approximately vertical, and then a jet of liquid is formed just forward of the crest of the wave. The jet develops and projects forward into a characteristic overturning motion (Fig.4(b)). Under the influence of gravity, the jet lengthens as it is "fed" from the primary flow and touches down on the forward face of the wave, entraining a pocket of gas (Fig.4(c)). The process is followed by forcing up a second jet, e.g. splash-up (Fig.4(d)) which in turn impinges on the forward face. The volume of gas enclosed beneath the splash-up is relatively small compared to that entrained by the first falling jet. As pushed forward by the plunging jet, the splash-up is growing in size (Fig.4(e)) and can rise as high as the the original plunging crest (not shown here). Once rising at the highest level, the splash-up loses most of its kinetic energy and its forward momentum, and moves back with respect to the original plunging jet, entraining a non-negligible amount of gas into the wave (Fig.4(f)). This entrained gas persists in the wave in the form of one relatively large bubble and several

small bubbles (Fig.4(g)). In our simulation we observed several successive splash-up cycles with a gradual decrease of the potential energy from one cycle to the next, as shown in Fig.4(e). At $t = 8$, the wave loses most of its potential energy, splashing no longer occurs.

The breaking process described herein, including the wave overturning, the phenomenon of splash-up and the mode of gas entrainment, is generally in accordance with the laboratory observations of Bonmarin,[4] for deep-water plunging breaking waves. In addition, Bonmarin has observed in his laboratory experiments that the first splash-up can rise as high as the original plunging crest (c.f. his figures 22 and 23), which may provide a validation of our numerical finding. More recently, Perlin *et al.*,[13] have made measurements of highly resolved surface elevations in a deep-water plunging breaker. Our simulation resembles also very nicely their images of post-breaking process, e.g. splash-up and subsequent evolution (M. Perlin, personal communication. Unfortunately these images are not shown in their paper).

B. Overturning motion

As shown in Fig.4 (b) and (c), the most characteristic feature of a plunging breaker is the overhanging jet of liquid that forms near the crest of the wave and plunges forward into the surface below. Progress has been made towards an analytical time-dependent description of various parts of the flow in irrotational plunging, breaking waves. For instance, Longuet-Higgins[30] proposed a simple self-similar cubic solution which fits the forward face of a plunging breaker while New[31] found that the curve of underside or loop of a plunging jet is often well described by an ellipse with axes in the ratio $\sqrt{3}$. Both of models, however, accounted for only a limited region of the loop and not for the rest of wave. An advance has been made by Greenhow[32] who extended and modified the ellipse model of New and the jet model of Longuet-Higgins to include the rest of the wave. Note that the flow in plunging breakers has sometimes been approximated by a stationary flow pattern (see, for example, Dias and Tuck[33] and Jenkins[34]).

Time-dependent numerical simulations of irrotational waves as they overturn and form jet have been performed by a number of authors.[6,11,12,26–29] Full details of the wave profile, velocity and pressure fields in waves during the overturning process up to the instant when the jet

is about to impinge into the forward face are obtainable from these detailed unsteady numerical computations. The most remarkable feature discovered from those computations[11,26,29] is that a region of large fluid accelerations, corresponding high pressure gradients, develops on the front face of a wave. Typical computed maxima are as high as five or six times that due to gravity.

Our results of velocity and acceleration fields during the overturning process have qualitatively similar feature as previous irrotational computations. A typical result is illustrated in Fig.5, showing the velocity field (Fig.5(a)) and corresponding accelerations in the region around the crest of wave at $t = 1.2$. From this figure one may classify three regions of particular interest: (i) high particle velocities in the prominent jet: the largest velocity magnitude is 0.68 and its horizontal component is 0.67 which is up to 45% greater than the phase speed of the wave (the phase speed of the initial wave is 0.46); (ii) high particle accelerations on the underside of the jet: the maximum acceleration is 3.25 times larger than that due to gravity and directed approximately towards the center of curvature of the overturning loop; (iii) low particle accelerations having negative horizontal component on the rear face. As can be seen, the jet seems to be formed and projected forward by some convergence of the flow. Also, it is noticed that large accelerations do not occur at the jet tip but within the jet with magnitude being relatively greater than that due to gravity.

Fig.6 shows the velocity field and magnified view of the acceleration field in the late stage of the wave overturning process at $t = 1.4$, that is, just priori to the "touchdown" of the jet on the forward face. It can be seen that the three regions mentioned above remain. The largest velocity, which is located in the jet, is 0.83 with horizontal component equal to 0.81, i.e. 76% greater than the phase speed of the wave. The most striking feature revealed from Fig.6(b) is that while the most part of the jet has downward acceleration, the accelerations near the jet tip are directed upward and forward. This is due to the gas entrained beneath the plunging jet which develops high pressure in the region between the tip of the jet and its forward face. On the other hand, these upward accelerations, i.e. the particle velocities decrease with time, are also expected because the jet is approaching to impinge on the surface below and to splash.

It is possible to compare our Navier-Stokes simulation with potential-flow theory. Indeed, we have also developed a potential-flow code using a boundary integral formulation. The numerical model is similar to that developed by Vinje and Brevig,[27] but viscosity and surface tension are accounted for in the computations. A full description of the formulation and computations will be reported elsewhere. Here, we just mention that the effect of viscosity is included in the computations by using boundary-layer theory as formulated by Lundgren and Mansour.[35]

Fig.7 shows the wave profiles and velocities along the free surface which are obtained respectively from Navier-Stokes simulation (Fig.7(a)) and potential-flow theory (Figs.7(b) and (c)). The computations with potential-flow theory are performed by using the same initial condition as in the Navier-Stokes simulation. Fig.7(b) corresponds to the Bond number $B = 10^4$ and the Reynolds number $Re = 10^4$ (as in the Navier-Stokes simulation), while Fig.7(c) is the classic potential-flow computation in which viscosity and surface tension are neglected. It is seen that up to the point of the jet re-entry onto the forward surface potential-flow theory with surface tension taken into account models the flow as good as the Navier-Stokes simulation. Indeed, two quite different models yield qualitatively similar wave profile and velocity distribution along the free surface. The main discrepancy between two computations lies in the size of the enclosed gas; the potential-flow theory tends to give a larger volume, but the difference in the maximum velocity is only about 1%. It should be pointed out that a smaller volume of the enclosed gas can be expected in a two-phase flow simulation due to the frictional and inertial influences of the gas surrounding the jet which are not accounted for in the potential-flow computations. The effect of surface tension on the shape of the plunging jet is clearly illustrated in Fig.7(b) compared to (c): the jet exhibits a rounded tip, rather than a sharp cusp as displayed in Fig.7(c).

Also shown in these figures (dashed lines) are the ellipses of aspect ration $\sqrt{3}$ which are fitted numerically using a technique based on the method of least squares. Such ellipse solution has been found by New.[31] It can be seen that when neglecting surface tension (Fig.7(c)) the profile of the underside of the overturning crest is indeed well approximated by a $\sqrt{3}$ aspect-ratio ellipse. The length of the major axis and its inclination to the horizontal

$x-$direction are respectively $a = 0.05$ and $\theta = -35^o$ which are in the range of values obtained by New.[31] We note that even in the Navier-Stokes simulation large portion of the underside of the plunging jet still displays approximately a $\sqrt{3}$–aspect-ratio ellipse having a smaller length of the major axis ($a = 0.03$) and a steeper angle ($\theta = -40^o$).

C. Phenomenon of splash-up

Once the plunging jet hits the liquid in front of the breaking wave, a sequence of splashes is created. Fig.8 shows the occurrence of the splash-up (Fig.8(a)) and the subsequent evolution of the wave (Fig.8(b)). It is clear that the splash-up starts from the plunge point, i.e. the place and instant of time where the falling jet touches forward undisturbed surface. The liquid in splash-up must come partly from the jet and partly from previously undisturbed liquid. However, a close inspection of the velocity fields shown in Fig.8 reveals that in the early stage the liquid in the splash-up originates from the plunging crest; the previously undisturbed surface acting like a solid surface. Indeed, the resulting splash has very large forward velocity component, i.e. 1.0. However, in the late stage of the splash-up, the jet penetrates the surface below and then, because of its forward motion and downward momentum, it pushes up a portion of previously undisturbed liquid, contributing to the development of the initial splash-up. It appears from the velocity field shown in Fig.8(b) that most of liquid in the splash-up comes from the previously undisturbed liquid.

One direct consequence of the impact of jet is the generation of vortex-like motions beneath the surface. The velocity field shown in Fig.8(b) suggests that there is essentially two large vortices, one around the entrained gas and another around the second entrained gas within the splash-up. Since these rotate in the same direction, the regions between them must have high shear rates, which result in a high rate of energy dissipation in these regions.

D. Entrainment of gas

The most obvious and important entrainment of gas arises from the closing of the jet on the lower surface (see Fig.8). Gas entrainment process occurs also at each successive splash-up

cycle, the amount of gas entrained decreasing from one splash-up to the next one.

The interaction between the plunging jet and the rear part of the splash-up contributes to a non-negligible amount of gas entrainment (see Fig.4(f) and (g)). This interaction can display two modes: in the early stage, the falling crest and the rear part of the splash-up turn in opposite direction, and subsequently, the splash-up attains the maximum elevation and looks like a falling liquid jet moving backwards and penetrating the front of the original breaking crest as it moves forward. These two modes of gas entrainment resulting from the interaction of the plunging jet and the rear part of the splash-up are consistent with the laboratory observations by Bonmarin.[4]

The processes of wave evolution and gas entrainment have considerable dynamical coupling. Air entrainment measurements in laboratory by Lamarre and Melville[36] suggest that a large fraction (up to 50%) of the surface wave energy dissipated is expended in entraining air against buoyancy forces.

E. Generation of vorticity

The vorticity field ω is defined in a usual way and can be easily obtained from the velocity filed (u, v):

$$\omega = \frac{\partial v}{\partial x} - \frac{\partial u}{\partial y}. \tag{14}$$

Fig. 9 shows the time history of the maximum positive vorticity (+) in the liquid phase. Though an initially irrotational motion is set in the bulk of each phase, a small amount of the vorticity, i.e. $\omega_{max} \approx 2$, does exist at the liquid/gas interface. This is because that at $t = 0$, there is a discontinuity in tangential velocity across this boundary, which is in fact equivalent to a sheet vortex at the interface. The vorticity is equal in magnitude to the local jump in tangential velocity and is thus finite. As time goes on, several effects determine the vorticity distribution. First, the vorticity which was concentrated at the interface at $t = 0$ diffuses into the fluid by the action of viscosity. It can be shown that at small values of t, the vorticity is within a layer of thickness of order $(\nu t)^{1/2}$ near the interface. Secondly, convection is able to transport vorticity toward or away from the interface. Third effect is

the local distortion and rotation of the fluid which modifies the local vorticity.

Fig.9 shows that the maximum vorticity increases approximately as a linear function of time up to the impact of jet ($t \approx 1.5$). A typical vorticity field during the overturning process is illustrated in Fig. 10(a). In vorticity plots, positive contours are shown by solid lines, while negative contours are shown by dashed lines with equally vorticity increment. It is seen that positive vorticity layer is mainly located at the tip of the jet, and negative vorticity layer is confined on the underside of the jet. The rest of the flow is essentially vorticity-free. Thus this vorticity distribution is consistent with the general remarks made before. A dramatical change in vorticity can be seen after the jet re-entry onto the forward surface. Indeed, the jet plunging on the surface below creates the vortical motion. But it is in the processes of splash-up that the largest vorticities are generated. Maxima can rise as high as 120. Fig. 10(b) suggests that strong vorticities are likely associated with the local (large) curvature of the interface. As this figure makes clear further, the gas entrapped by wave breaking has a direct consequence of the generation of vorticity: negative vorticity contours are essentially located around them.

Oscillations in the vorticity history in Fig.9 are due to successive splash-up cycles which take place during the breaking process. After $t > 6$, most of wave energy was dissipated, wave motion becomes again almost irrotational state.

The mechanisms responsible for generation of vorticity at a two-fluid interface has been discussed by Yeh.[37] He showed that there are only two mechanisms to create vortical motion (i.e. vorticity) at a two-fluid interface: baroclinic torque and viscous-shear torque. When surface-tension forces are included, an additional torque is possible due to the discontinuity in stress tensor at the interface. Also, it is well-known that curvature at a free surface generates locally intense vorticity. This mechanism has been investigated by Longuet-Higgins[38] who showed that in any steady flow in which the tangential stress vanishes, the strength of the vorticity is $2\kappa q$, where κ is the curvature of the streamline at the surface and q is the stream velocity. Vortex-like motions which appeared in breaking wave must have been created by those mechanisms. Though effect of the curvature of the interface seems to be the most important contribution of vorticity, a more detailed investigation would be necessary to

examine which mechanism is the dominant contribution to the source of vorticity.

F. Energy dissipation

Let T_L, V_L and Π denote respectively the wave kinetic energy, the wave (gravitational) potential energy and the surface-tension energy, which are calculated in the liquid part ($C \neq 0$) over one wavelength. Using the present reference scales, they are given by

$$T_L = \frac{1}{2} \int \int_{C \neq 0} \rho \mathbf{u}^2 dx dy, \tag{15}$$

$$V_L = \int \int_{C \neq 0} \rho y dx dy + \frac{1}{8}, \tag{16}$$

$$\Pi = \frac{1}{B}(\Gamma - 1), \tag{17}$$

where Γ is the total arclength of liquid-gas interface. The constant $1/8$ appearing in equation (16) is introduced to define zero potential energy for a non perturbed surface.

The total wave (mechanical) energy, E, is then obtained by summing these three parts. It is well-known that due to the viscosity the total energy of an infinitesimal amplitude wave in deep depth decays as $\exp(-2\gamma t)$ and the amplitude as $\exp(-\gamma t)$, where the decay rate γ is defined by equation (11). For the purpose of comparison, we use the parameters given in Sec. IV and obtain $\gamma = 1.9 \times 10^{-2}$.

The time evolutions of normalized values (by its initial value) of E, T_L and V_L, are plotted in Fig. 11. The initial values of the energies are respectively $E = 4.9 \times 10^{-3}$, $T_L = 2.7 \times 10^{-3}$ and $V_L = 2.2 \times 10^{-3}$. The surface-tension energy is two orders of magnitude smaller than the gravitational potential energy and the kinetic energy ($\Pi(t = 0) = 1.1 \times 10^{-5}$): its contribution to the total wave energy is negligible, thus, its time evolution is not plotted in the figure. It is seen that the time evolutions of energies display distinctly different regimes before, during and after the breaking process. Before the formation of the jet ($t < 0.5$), the kinetic and potential energies decrease smoothly. After the formation of the jet and under the influence of gravity, the jet plunges down, the potential energy decreases rapidly and goes into kinetic energy, leading to increase the latter up to the time of impact of the

jet onto the forward surface ($t \approx 1.5$). The curves of T_L and V_L exhibit some oscillations due to the formation of successive splash-up cycles generated by the first falling jet; each fast decreasing of the potential energy is associated with a relatively increase in the kinetic energy and vice versa.

The total wave energy is dissipated by viscosity, thus decreases always with the time. Its evolution as shown in Fig. 11 is not a simple function of time. An attempt is made to determine a possible time dependence (exponential or algebraic). It is found that the curve of E actually exhibits three different slopes indicating different wave energy decay regimes. Fig. 12 summarizes our finding. Fig. 12(a) is a linear-log plot while Fig. 12(b) is a log-log plot. It is seen that during the wave evolution, plunging and breaking process, the the wave total energy follows approximately a classic exponential decay but has different decay rate. Before the impact of the jet ($t < t_1 = 1.5$), the decay rate is found to be $\gamma_1 = 3 \times 10^{-2}$. Relatively large decay rate, e.g. $\gamma_2 = 0.16$, is found during the breaking process ($t_1 < t < t_2 = 5.2$). This decay value is more than five times γ_1 and is eight times the linear decay rate γ that we mentioned. This indicates that the wave energy is mainly dissipated during the breaking process. At two wave periods after breaking, the total energy is found to follow approximately an algebraic decay. More precisely, the decay of the total energy with time is found to be proportional to t^{-1}. This t^{-1} dependence can be clearly seen in Fig. 12(b).

From Fig. 11, it is seen that after three wave periods about 30% of the kinetic energy and only a small percentage (5%) of the potential energy remain in the wave, and that more than 80% of the total pre-breaking wave energy is dissipated.

Using the dispersive properties of deep water waves to focus a wave packet in a laboratory channel, Melville and Rapp,[39] and Rapp and Melville[5] measured the wave momentum flux (or energy density) of the wave field upstream and downstream of the breaking region, thereby inferring the losses from the wave field due to breaking. The measurements of Rapp and Melville[5] show that more than 90% of the total prebreaking wave energy is dissipated after four wave periods (from the onset of breaking). From this time on, the kinetic energy in the residual flow is found to decay as t^{-1}. Our numerical results of energy dissipation and

t^{-1} dependence of total energy are comparable to their measurements. However, it should be stressed that we calculated the dissipation in a single breaking wave while Rapp and Melville[5] measured the dissipation in a wave group. Also, the inherent feature of our two-dimensional simulation may be the most important factor which leads to the discrepancy. It is well-known that the two-dimensional turbulence is less dissipative compared to three-dimensional turbulence as in their experiments. Indeed, in three-dimensions, a very small amount of viscosity suffices to produce a finite energy dissipation. While in two-dimensions, when the viscosity is small, so is the energy dissipation. Taking these into consideration, we may say that our numerical simulations are consistent with Rapp and Melville's laboratory measurements, and confirm that the turbulence generated by breaking is highly dissipative.

6. SUMMARY AND CONCLUDING REMARKS

Plunging breakers are due to the formation of a jet forward the crest of the wave. Under the influence of gravity the jet plunges down into the surface causing splashes, air entrainment and vortical motions beneath the surface. Classical numerical codes based on potential theory are unable to describe evolution of breaking waves beyond the point at which the jet impacts the surface. In this work, we employed a piecewise linear version of the volume of fluid method to simulate wave breaking as a two-phase flow. The incompressible, two-dimensional Navier-Stokes equations were directly solved with explicit tracking of the interface between the two phases. Numerical simulations of the evolution of an initially steep short gravity wave with surface tension captured most of dynamics of plunging breaking waves, and results are in reasonable agreement with laboratory observations for a deep-water wave breaking process, including wave overturning, plunging, air entrainment and successive splash-up cycles.

The generation of vorticity in breaking waves is due to the baroclinic torque and viscous shear torque. With surface tension taken into account vorticity can also be created in regions of large curvature of the interface due to the additional baroclinic generation term in the stress tensor at the interface, and diffused away from the immediate neighborhood of the interface by viscosity. Our calculations show that up to the appearance of the vertical front

face of the wave, the wave motion is quasi-irrotational. Then, as a localized vorticity layer develops near the tip of the liquid jet (positive vorticities) and along the underside of the jet (negative vorticities), the magnitude of the vorticity becomes appreciable. Nevertheless, the flow remains irrotational in most of the wave, and it is unlikely that the wave overturning process is much influenced by the rotational flow. In this regard, our Navier-Stokes calculations support previous potential-theory computations for wave evolution up to the jet re-entry onto the forward surface. Indeed, the velocity and acceleration fields obtained from the present work are qualitatively similar to those obtained from computations of potential flows. However, considerable vorticity is generated in the subsequent development of the wave breaking process. The most obvious of which is at the head of, and around, the tip of the injection jet after its entry into the surface below. A second source of vorticity is the shear layer formed between the falling jet and the rear part of splash-up moving upwards. The instability of this shear zone is also a source of high energy dissipation in breaking waves. The gas bubbles entrapped by wave breaking directly generate vorticity: negative vorticity contours are essentially located around them. Overall, we may say that the most striking effect of a breaking wave is the generation of rotational motions beneath the surface and the energy dissipation; the latter being a direct consequence caused by the former.

Our calculated velocity fields reveal that the splash-up commences from the plunge point, and that the origin of the splash-up comes first from the plunging crest which acts like a direct reflection on the undisturbed surface. Subsequently, the plunging jet pushes up the undisturbed liquid, feeding the splash-up. The most part of the liquid in splash-up arises from this process.

Different decay regimes of the total wave energy with time were found. In the early stage of the breaking process, the total energy follows approximately two different exponential decays with a relative large decay rate during splash-up. After two wave time periods, the total energy follows an algebraic decay and was found to have a t^{-1} dependence. More than 80% of the total pre-breaking wave energy was dissipated within three wave periods.

The results highlight the power of advanced numerical techniques to unveil the fascinating complexity involved in wave breaking process (splash-up, vortex-like motion and gas

entrainment). However, difficulties remain with such calculations. First difficulty is the slow convergence with the number of grid points. The lower resolution experiments produce a similar breaking process as provided by higher resolution ones, the main difference being in smaller structures created in the former. This phenomenon is clearly illustrated in Fig.13 where we try to compare the results obtained with two different resolutions (256×256 and 512×512). Indeed, the breaking phenomenon tends to create structures of very small size (such as droplets, see Fig.13(a)) because of the systematic stretching of a thin filament of liquid as shown in Fig.13(b). If and when these structures reach sizes smaller than the mesh size, a loss of accuracy occurs. With a higher resolution, capillary effects which are relatively important in these small structures are more captured and resolved, the interface is thus more stable. However, the overall dynamics of breaking waves are unlikely affected by these smaller structures. A quantitative comparison of the numerical results obtained with two different resolutions is shown in Fig.14 where we plot the time evolutions of the total wave energy. It is seen that before the impact of the jet ($t < t_1 = 1.5$) and after two wave time periods ($t > t_2 = 5.2$) the results obtained are almost indistinguishable between two resolutions. The differences occur during the breaking process, but the maximum relative error between two resolutions is within 10%. From this figure, it is worth noting that the amount of the total wave energy dissipation is unchanged, indicating to some extent the convergence reached by the present resolution, i.e. 512×512 grid points. A second difficulty is the two-dimensional nature of these computations. As is well known, coherent vortical structures and cascade to smaller scales are quite different in two with respect to three dimensions, and hence so should evolution of the vorticity field and energy dissipation. Despite these difficulties, the present numerical simulation of breaking waves is promising. Comparison of the numerical results with some laboratory experiments is encouraging, and we regard two-dimensional simulations as a very useful warmup for more realistic three-dimensional investigations. The ability of the code to simulate the dynamics of the gas phase also offers the perspective of simulating breaking waves in presence of wind.

ACKNOWLEDGMENTS

The authors wish to thank Prof. D.H. Peregrine for his helpful comments and suggesting improvements to an early draft of the manuscript, and Dr. P. Bonmarin for stimulating discussions. We would also like to thank anonymous reviewers of this paper for their helpful comments. The computations were done on the SGI Power Challenge at IRPHE and in part on the SP2 of the CNUSC (Centre National Universitaire du Sud de Calcul). The support from DRET (Direction des Recherches, Etudes et Techniques) is gratefully acknowledged.

REFERENCES

1. W. K. Melville, "The role of surface-wave breaking in air-sea interaction," Annu. Rev. Fluid Mech. **28**, 279 (1996).

2. M. L. Banner and W. K. Melville, "On the separation of air flow over water waves," J. Fluid Mech. **77**, 825 (1976).

3. J. H. Duncan, "An experimental investigation of breaking waves produced by a towed hydrofoil," Proc. R. Soc. London Ser. A **377**, 331 (1981).

4. P. Bonmarin, "Geometric properties of deep-water breaking waves," J. Fluid Mech. **209**, 405 (1989).

5. R. J. Rapp and W. K. Melville, "Laboratory measurements of deep-water breaking waves," Philos. Trans. R. Soc. London Ser A **331**, 735 (1990).

6. M. S. Longuet-Higgins and E. D. Cokelet, "The deformation of steep surface waves on water. I. A numerical method for computation," Proc. R. Soc. London Ser. A **358**, 1 (1976).

7. M. S. Longuet-Higgins and E. D. Cokelet, "The deformation of steep surface waves on water. II. Growth of normal-mode instabilities," Proc. R. Soc. London Ser. A **364**, 1 (1978).

8. W. J. Jillians, "The superharmonic instability of Stokes waves in deep water," J. Fluid Mech. **204**, 563 (1989).

9. D. H. Peregrine, "Breaking waves on beaches," Annu. Rev. Fluid Mech. **15**, 149 (1983).

10. M. L. Banner and D. H. Peregrine, "Wave breaking in deep water," Annu. Rev. Fluid Mech. **25**, 373 (1993).

11. D. G. Dommermuth, D. K. P. Yue, W. M. Lin, R. J. Rapp, E. S. Chan and W. K. Melville, "Deep-water plunging breakers: a comparison between potential theory and experiments," J. Fluid Mech. **189**, 432 (1988).

12. D. Skyner, "A comparison of numerical predictions and experimental measurements of the internal kinematics of a deep-water plunging wave," J. Fluid Mech. **315**, 51 (1996).

13. M. Perlin, J-H. He and L. P. Bernal, "An experimental study of deep water plunging breakers," Phys. Fluids **8**, 2365 (1996).

14. J. J. Monaghan, P. J. Bicknell and R. J. Humble, "Volcanos, tsunamis and the demise of the minoans," Physica D **77**, 217 (1994).

15. C. W. Hirt and B. D. Nichols, "Volume of Fluid (VOF) method for the dynamics of free boundaries," J. Comput. Phys. **39**, 201 (1981).

16. D. L. Youngs, "Time dependent multimaterial flow with large fluid distortion," In *Numerical methods for fluid dynamics*, edited by K. M. Morton and M. J. Baines (Academic, New York, 1982) p. 27.

17. J. M. Hyman, "Numerical methods for tracking interfaces," Physica D **12**, 396 (1984).

18. J. .M. Floryan and H. Rasmussen, "Numerical methods for viscous flows with moving boundaries," Appl. Mech. Rev. **42**(12), 323 (1989).

19. N. Ashgriz and J. Y. Poo, "FLAIR: Flux line-segment model for advection and interface reconstruction," J. Comput. Phys. **93**, 449 (1991).

20. E. G. Puckett and J. S. Saltzman, "A 3d adaptive mesh refinement algorithm for interfacial gas dynamics," Physica D **60**, 84 (1992).

21. B. Lafaurie, C. Nardone, R. Scardovelli, S. Zaleski and G. Zanetti, "Modelling merging and fragmentation in multiphase flows with SURFER," J. Comput. Phys. **113**, 134 (1994).

22. J. Li, "Calcul d'interface affine par morceaux (piecewise linear interface calculation)," C. R. Acad. Sci. Paris, série IIb **320**, 391 (1995).

23. A. J. Chorin, "Numerical solution of the Navier-Stokes equation," Math. Comput. **22**, 745 (1968).

24. W. H. Press and S. A Teukolsky, "Multigrid methods for boundary value problems," Comput. Phys. Sep/Oct, 514 (1991).

25. H. Lamb, *Hydrodynamics,* 6th ed. (Cambridge University Press, 1932).

26. D. H. Peregrine, E. D. Cokelet and P. McIver, "The fluid mechanics of waves approaching breaking," *Proceedings of the 17th Coastal Engineering Conference,* Sidney, Australia, 1980, Vol. 1, p. 512.

27. T. Vinje and P. Brevig, "Numerical simulation of breaking waves," Adv. Water Resources **4**, 77 (1981).

28. G. R. Baker, D. I. Meiron and S. A. Orszag, "Generalized vortex methods for free-surface flow problems," J. Fluid Mech. **123**, 477 (1982).

29. A. L. New, P. McIver and D. H. Peregrine, "Computations of overturning waves," J. Fluid Mech. **150**, 233 (1985).

30. M. S. Longuet-Higgins, "Parametric solutions for breaking waves," J. Fluid Mech. **121**, 403 (1982).

31. A. L. New, "A class of elliptical free-surface flows," J. Fluid Mech. **130**, 219 (1983).

32. M. Greenhow, "Free-surface flows related to breaking waves," J. Fluid Mech. **134**, 259 (1983).

33. F. Dias and E. O. Tuck, "A steady breaking wave," Phys. Fluids A **5**, 277 (1993).

34. A. D. Jenkins, "A stationary potential-flow approximation for a breaking-wave crest," J. Fluid Mech. **280**, 335 (1994).

35. T. S. Lundgren and N. N. Mansour, "Oscillations of drops in zero gravity with weak viscous effects," J. Fluid Mech. **194**, 479 (1988).

36. E. Lamarre and W. K. Melville, "Air entrainment and dissipation in breaking waves," Nature **351**, 469 (1991).

37. H. Yeh, "Vorticity generation at a fluid interface," *Proceedings of the IUTAM Symposium*

on breaking waves, edited by M. L. Banner and R. H. J. Grimshaw (Springer-Verlag, 1991), p. 257.

38. M. S. Longuet-Higgins, "Capillary rollers and bores," J. Fluid Mech. **240**, 659 (1992).

39. W. K. Melville and R. .J. Rapp, "Momentum flux in breaking waves," Nature **317**, 514 (1985).

FIGURES

Fig. 1. Coordinate system and schematic drawing of initial interface profile $\eta(x, t = 0)$. In the simulations described in this paper, we have used periodic boundary condition in the direction of wave propagation and free-slip condition along the others.

Fig. 2. Simulation of small-amplitude capillary waves on the interface between two viscous fluids. (a) The ratio of the measured frequency to the predicted one (equation (9)) as a function of the mesh size h $(= 1/N$, where N is the number of grid points along one direction), (b) Time evolution of the interface position at $x = 0$, obtained from computation with grid size of 128×128. The dashed curve is the predicted viscous envelope in the inviscid linear theory, i.e. $\eta(0, 0)exp(-\gamma t)$, where the decay rate γ is given by equation (10).

Fig. 3. Simulation of small-amplitude gravity waves propagating on the interface between two viscous fluids. The solid curve is the time evolution of the interface position at $x = 0$. The dashed curve is the predicted viscous envelope in the inviscid linear theory, i.e. $\eta(0, 0)exp(-\gamma t)$, where the decay rate γ is given by equation (11). (a) computation with 128×128 grid points, (b) computation with 256×256 grid points.

Fig. 4. Snapshots of time sequence of a plunging breaking wave. Displayed region is $-0.5 \leq x \leq 0.5$ (corresponding to one wavelength) and $-0.3 \leq y \leq 0.3$. Physical parameters and initial conditions are given in the text. (a) $t = 0.56$, (b) $t = 1.2$, (c) $t = 1.44$, (d) $t = 1.76$, (e) $t = 2.08$, (f) $t = 2.96$, (g) $t = 5.76$, (h) $t = 8.0$.

Fig. 5. Close-up of the active region during the wave overturning at $t = 1.2$. The liquid-gas interface is represented by bold line. (a) Velocity field. The velocity vectors are plotted in every four computational cells. The largest velocity magnitude is 0.68 and its horizontal component is 0.67. (the phase speed of the initial wave is 0.46); (b) acceleration. Maximum acceleration is 3.25 which is located on underside of the overhanging jet and directed out of the fluid. The reference of acceleration is such that the gravitational acceleration g is equal to unity.

Fig. 6. The overturning process at $t = 1.4$, priori to the impingement of the jet on the forward face. (a) Velocity field. The largest velocity magnitude is 0.83 and its horizontal component is 0.81. (b) close-up of accelerations. Maximum acceleration is 3.62.

Fig. 7. Comparison between Navier-Stokes simulation with potential-flow theory using a boundary integral formulation. The dashed lines denote the $\sqrt{3}$ aspect-ratio ellipses, fitted numerically to the profiles of underside of the overturning crest. (a) Navier-Stokes simulation, The largest velocity magnitude is $U_{max} = 0.83$. (b) potential-flow theory computation with the effects of surface tension and viscosity taken into account. $U_{max} = 0.84$ (c) potential-flow theory computation without surface tension and viscosity. $U_{max} = 0.89$.

Fig. 8. Velocity fields near the plunge point at $t = 1.56$ (a) and at $t = 1.92$ (b), showing the occurrence of splash-up and the subsequent development. The maximum velocities are respectively 1.1 and 0.86

Fig. 9. Time history of the maximum vorticity (+).

Fig. 10. Contours of constant positive (slide line) and negative (dashed line) vorticity at $t = 1.4$ (a) $\omega_{min} = -17.3$, $\omega_{max} = 49.8$, and at $t = 1.92$ (b) $\omega_{min} = -85.2$, $\omega_{max} = 88.1$. Contours are in increments of $(\omega_{max} - \omega_{min})/18$ from the minimum vorticity ω_{min}.

Fig. 11. (a)Time evolutions of the total wave energy (E, solid line), the wave kinetic energy (T_L, dashed line) and the wave potential energy (V_L, dashdot line). Each energy is normalized by its initial value.

Fig. 12. Different decays of the total wave energy with time. Numerical results are represented by +. (a) Exponential decay. Plotted solid line is a fit function given by $exp(-2\gamma_1 t)$ ($\gamma_1 = 0.03$ and $t < t_1 = 1.5$). The dashed line represents a fit function given by $E(t = t1)exp(-2\gamma_2(t - t_1))$ ($\gamma_2 = 0.16$, $t_1 < t < t_2 = 5.2$). (b) Algebraic decay after two wave periods. The solid line is a fit function given by $E(t = t_2)t_2/t$ ($t > t_2$).

Fig. 13. Comparison of two different resolutions. (a) 256×256 grid points; and (b) 512×512 grid points.

Fig. 14. Time evolutions of the total wave energy E obtained with two different resolutions. (a) 256×256 grid points (dashed line); and (b) 512×512 grid points (solid line).

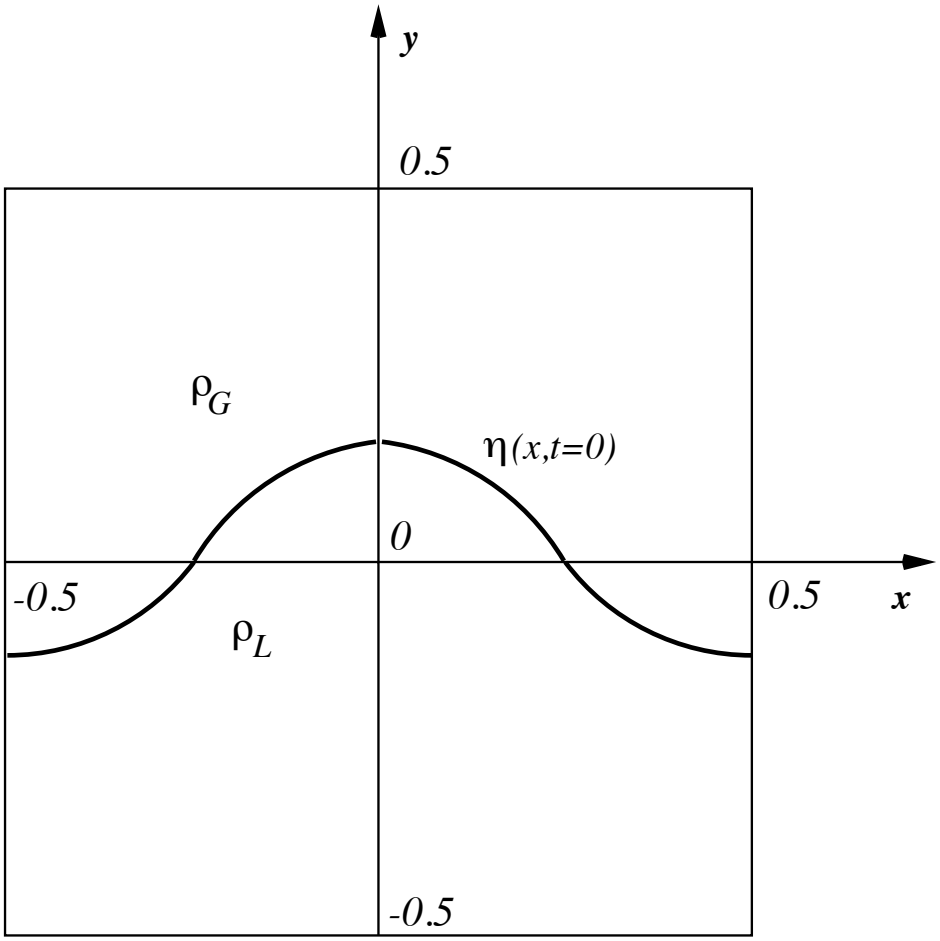

Fig.1 Chen et al.

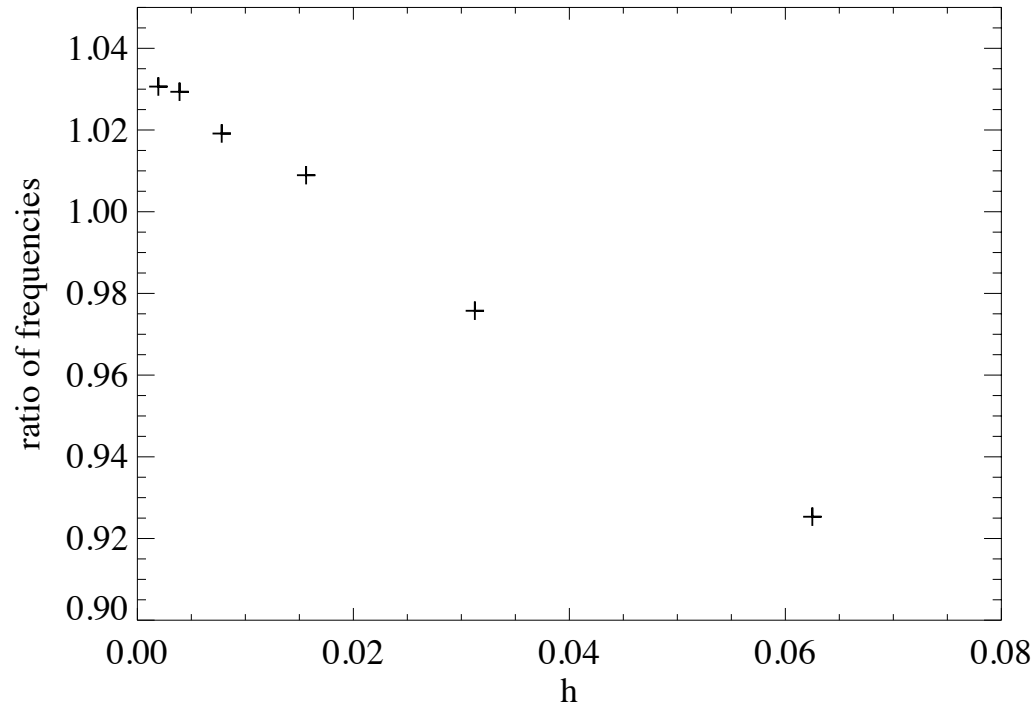

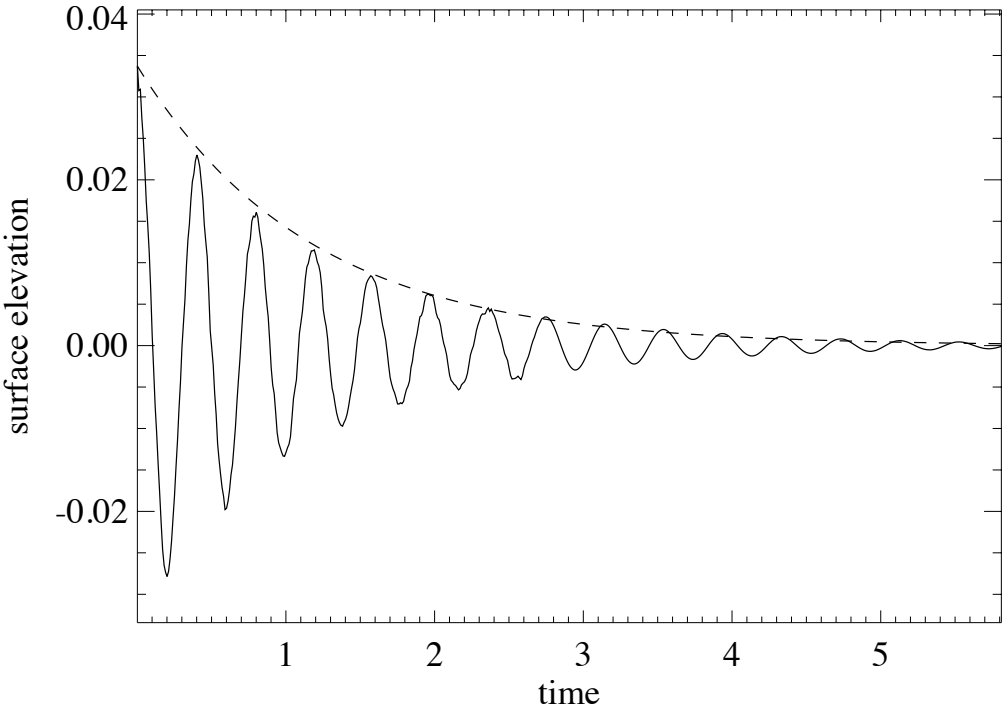

Fig.2 Chen et al.

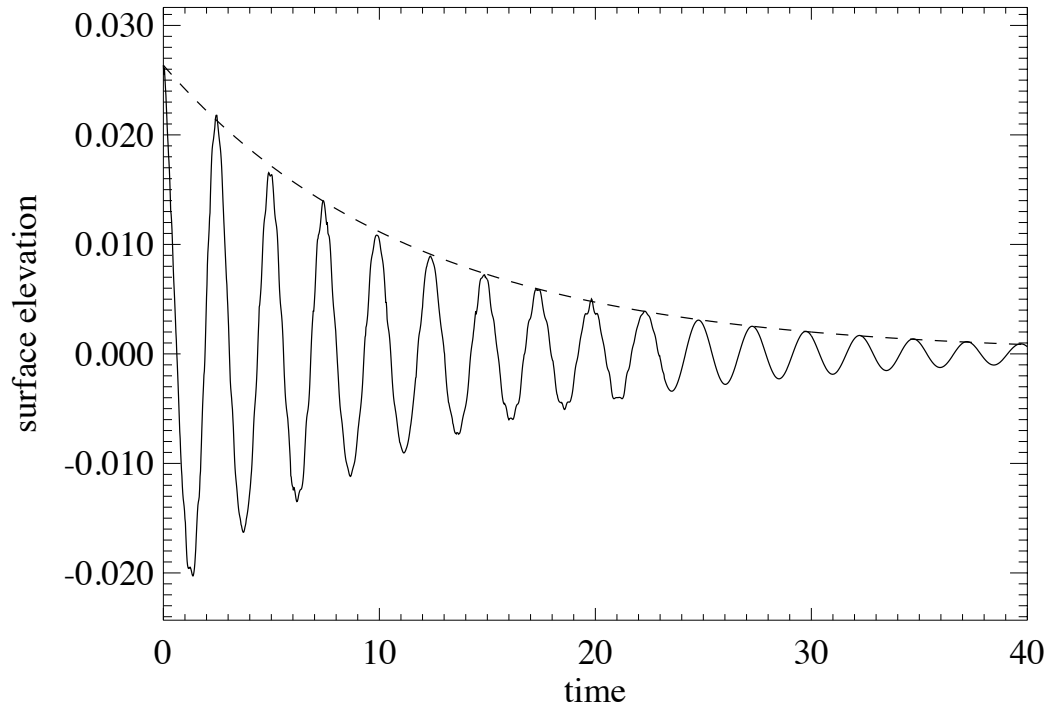

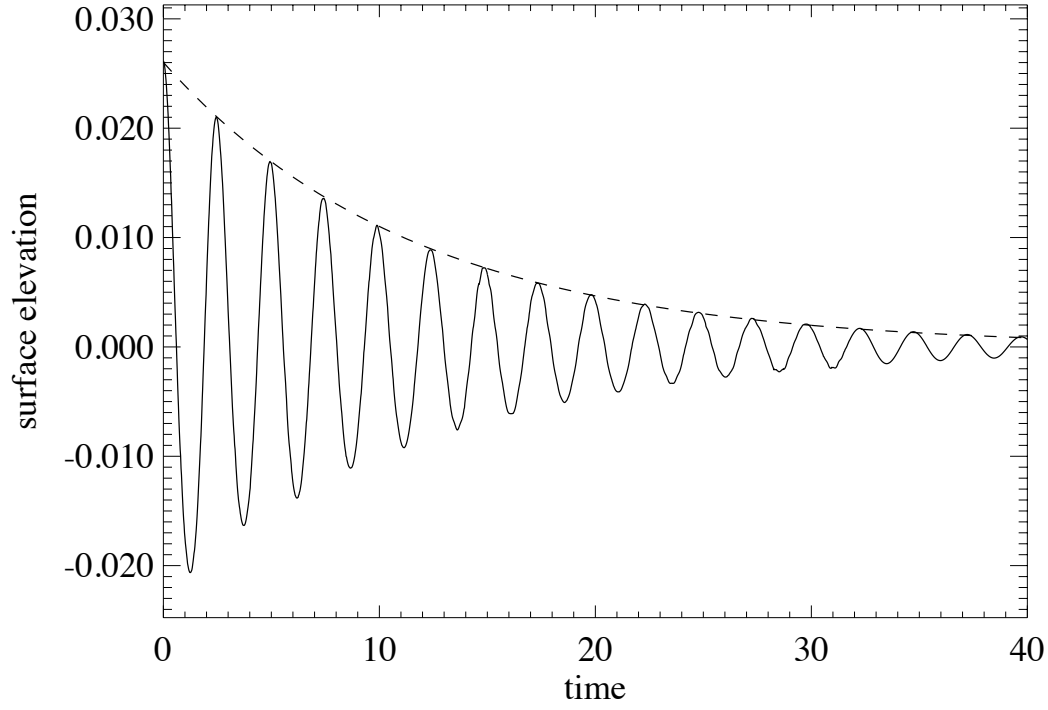

Fig.3 Chen et al.

(a)

(e)

(b)

(f)

(c)

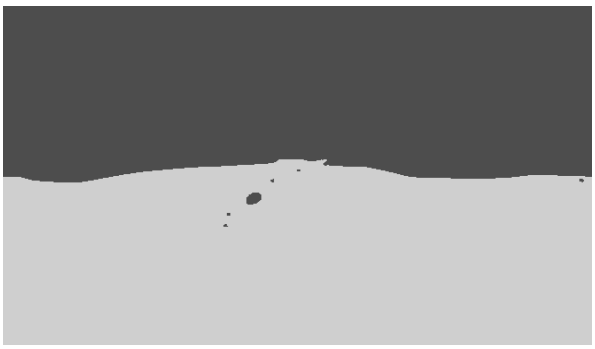

(g)

(d)

(h)

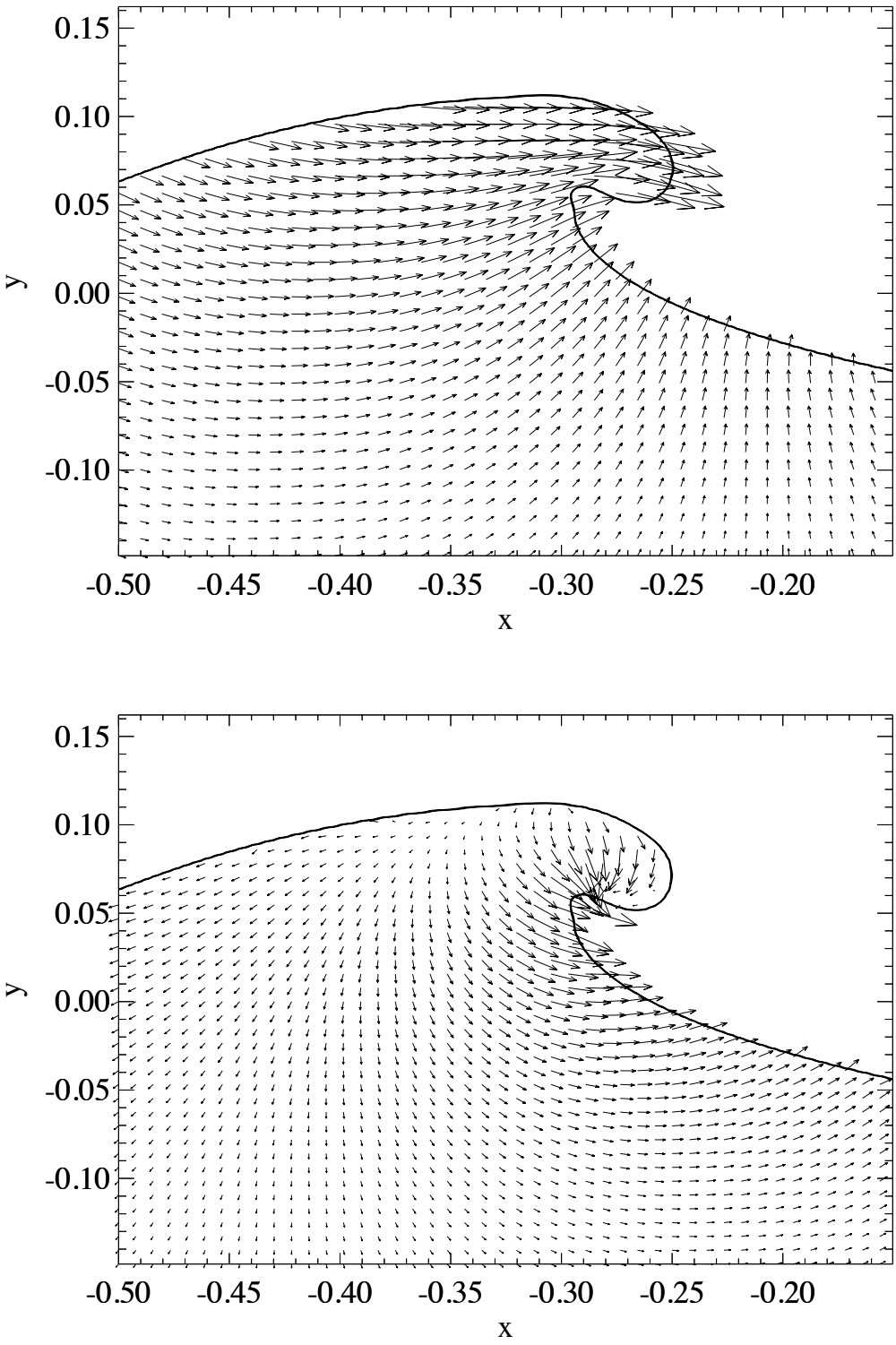

Fig.5 Chen et al.

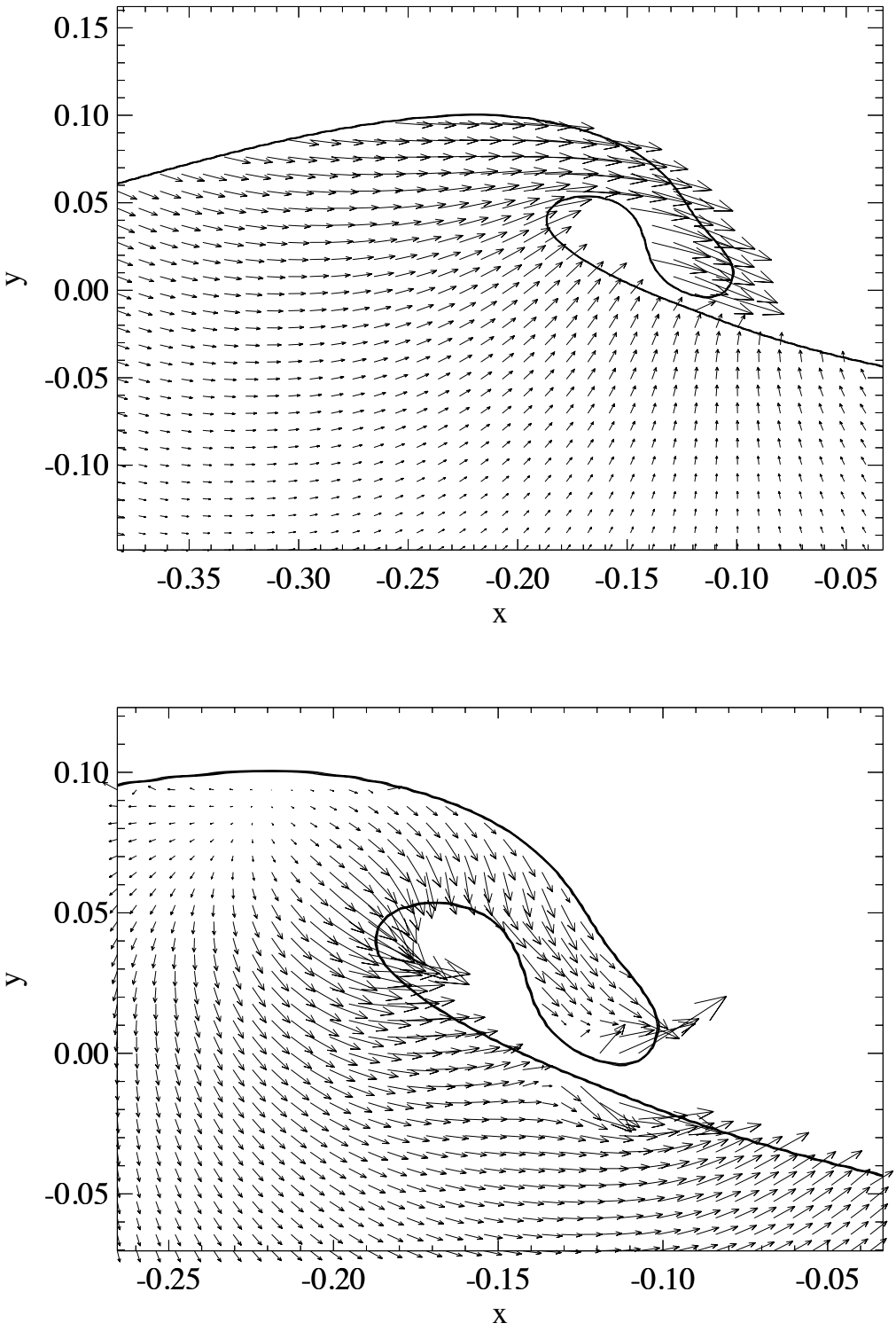

Fig.6 Chen et al.

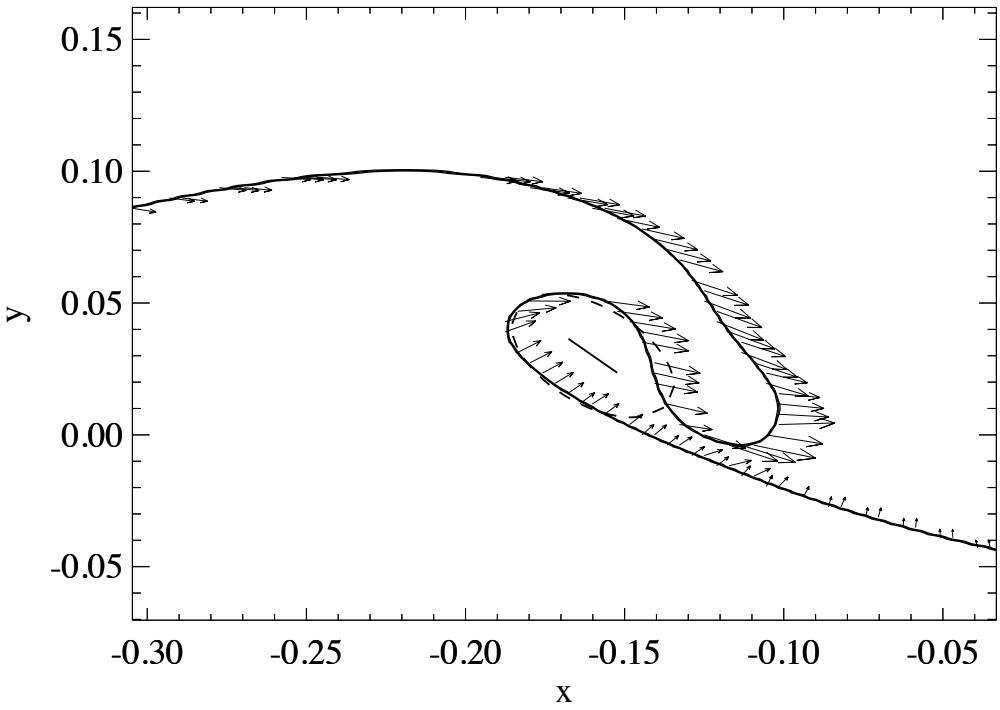
0.15
0.10
0.05
0.00
-0.05
y
-0.30
-0.25
-0.20
-0.15
-0.10
-0.05
x

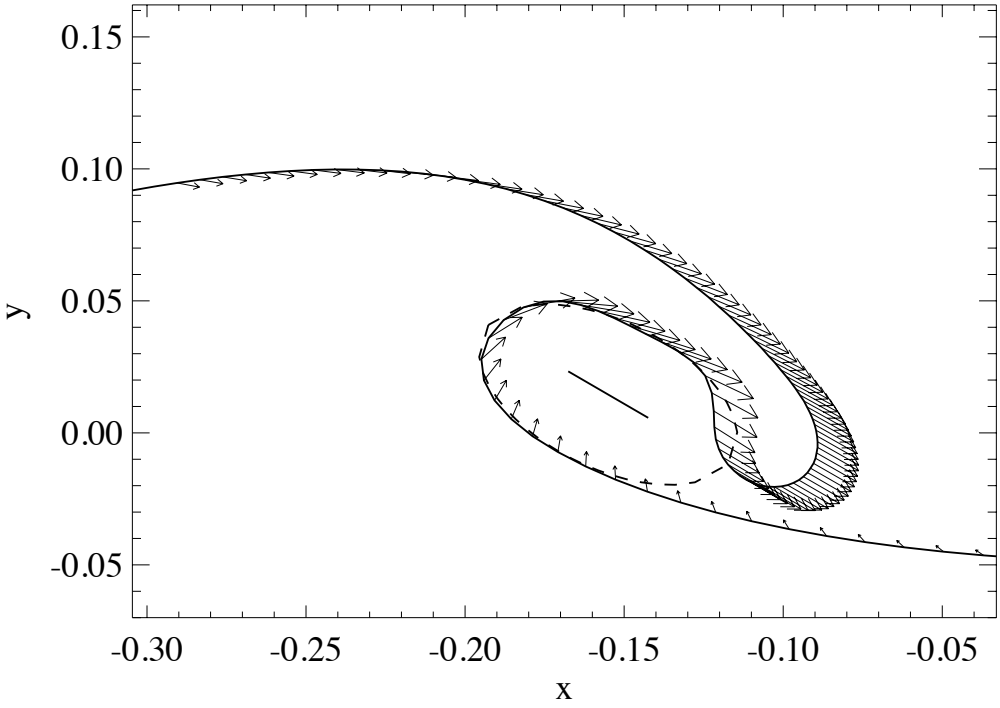
0.15
0.10
0.05
0.00
-0.05
y
-0.30
-0.25
-0.20
-0.15
-0.10
-0.05
x

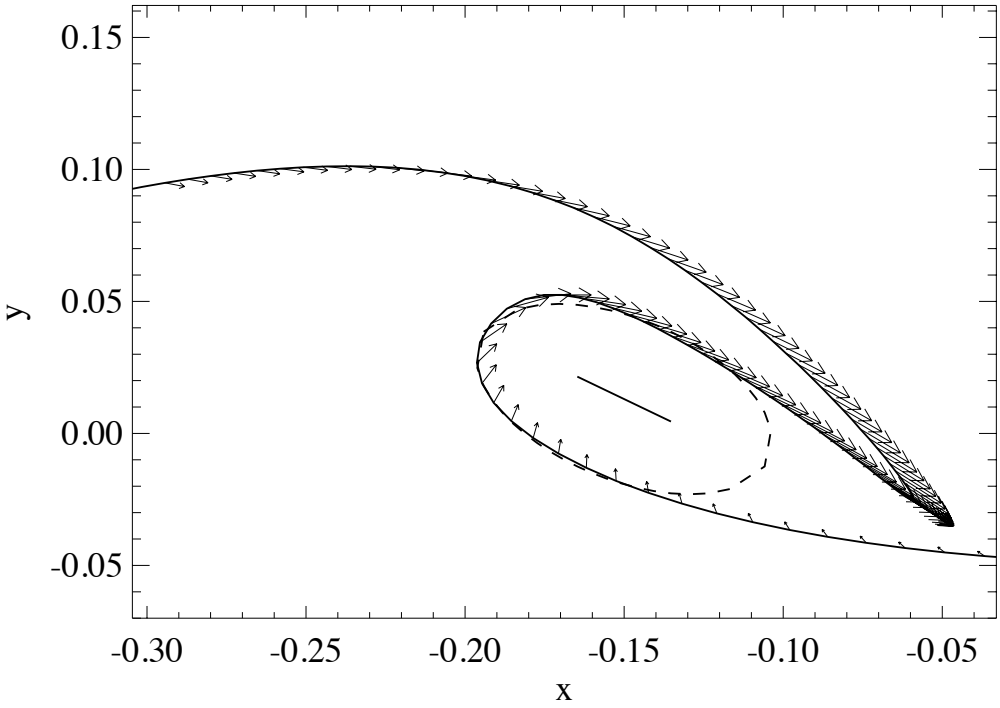

Fig.7 Chen et al.

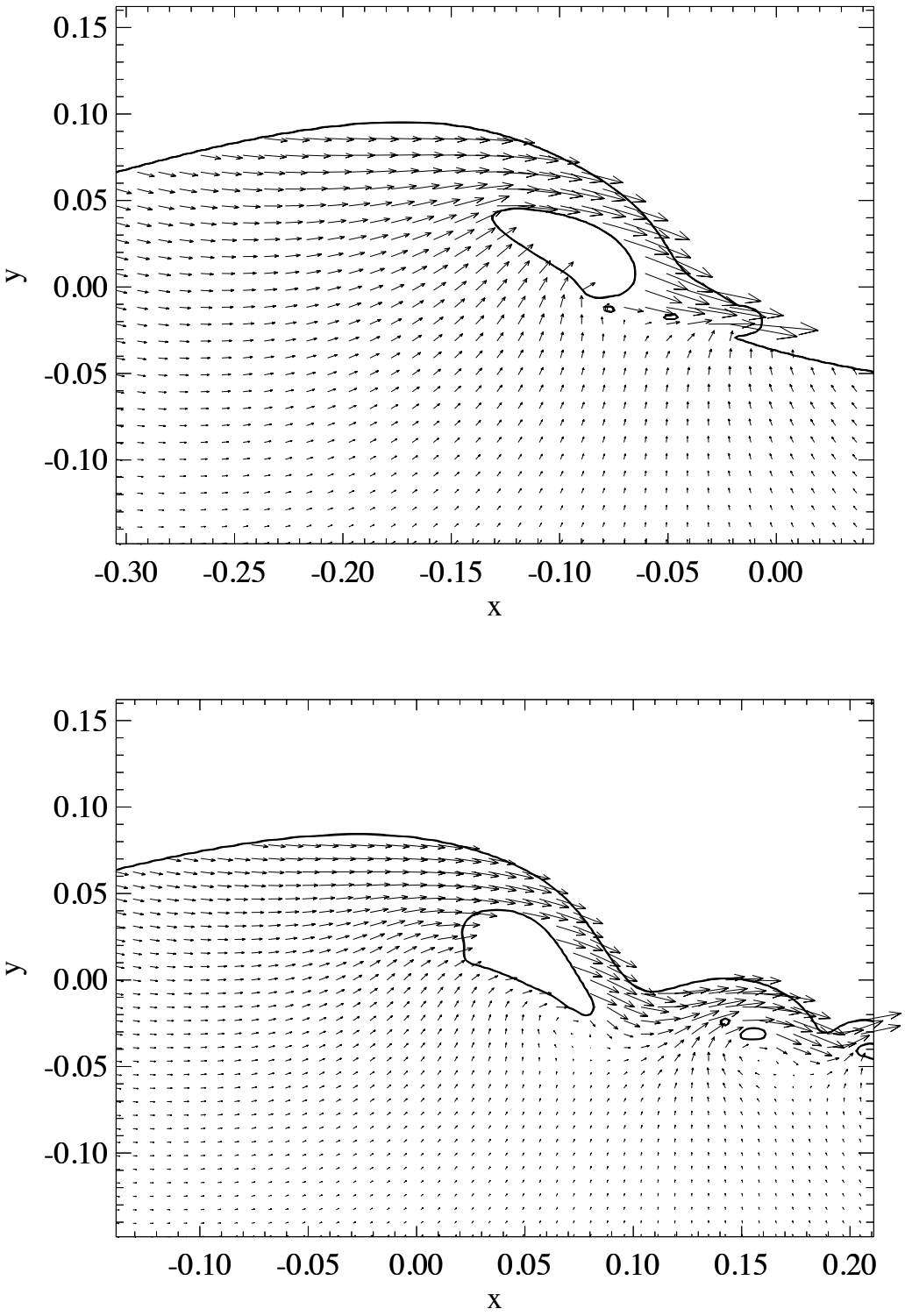

Fig.8 Chen et al.

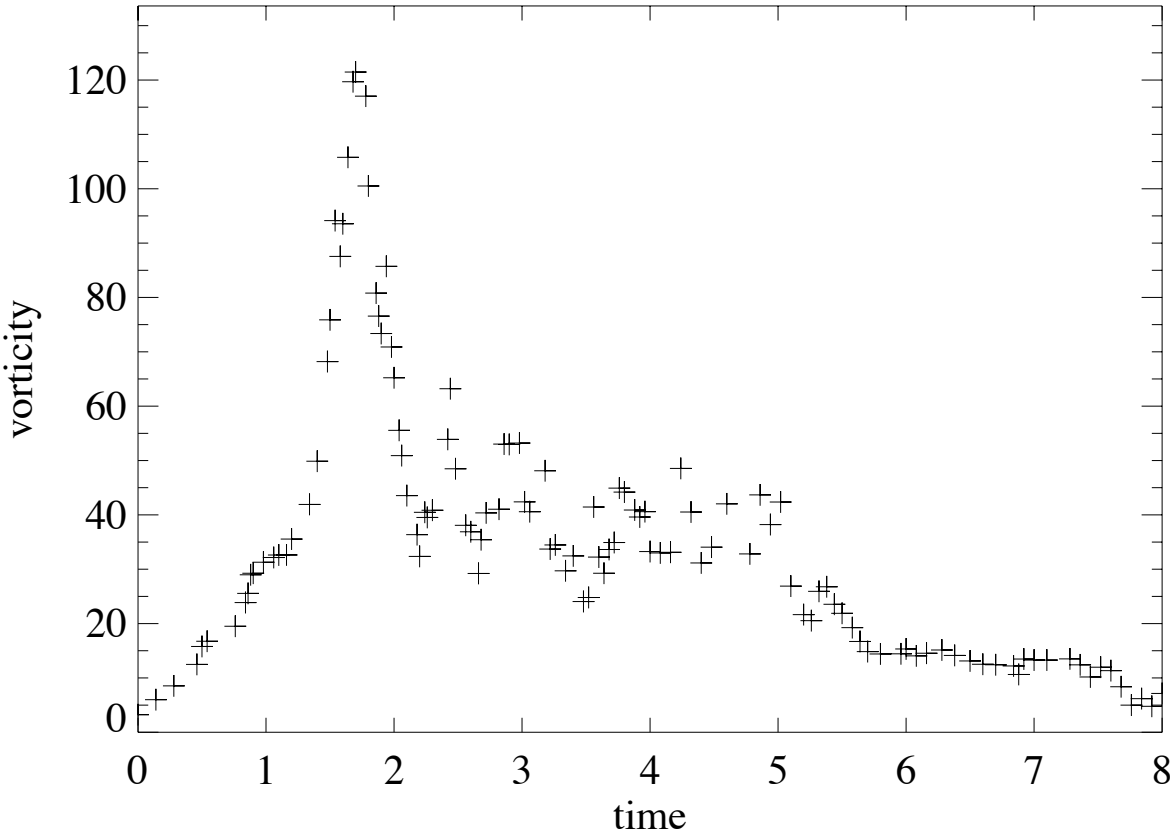

Fig.9 Chen et al.

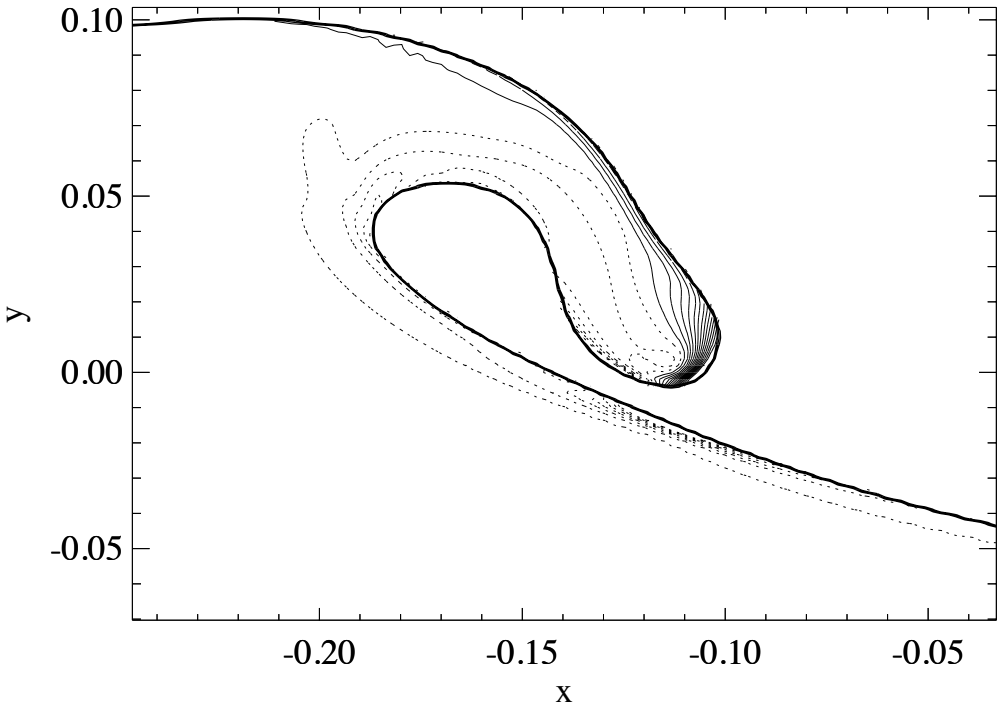

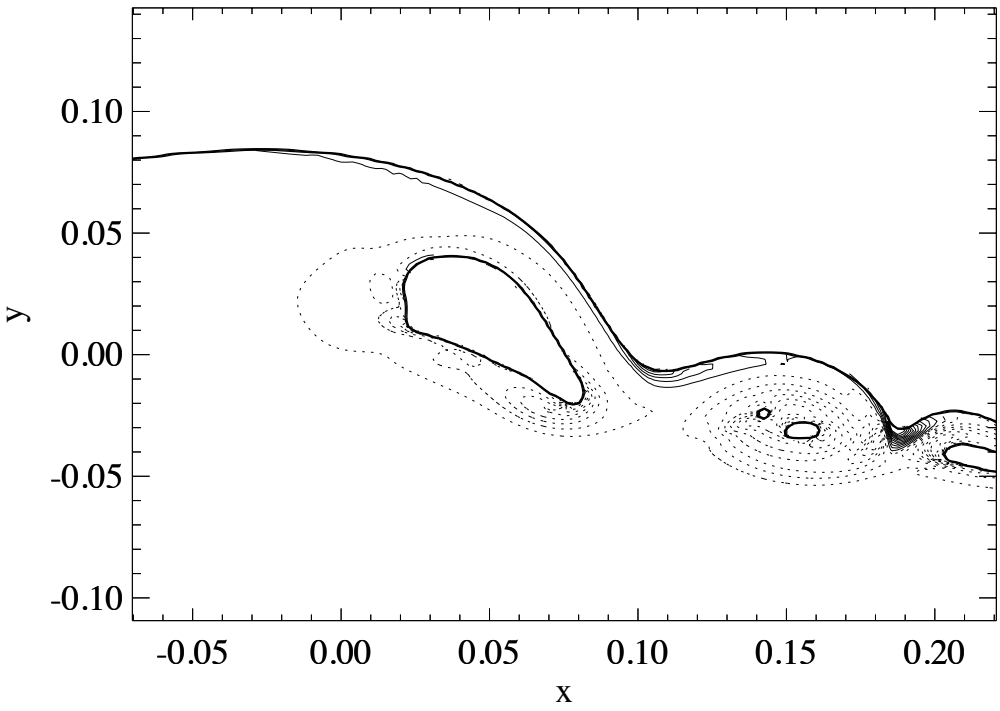

Fig.10 Chen et al.

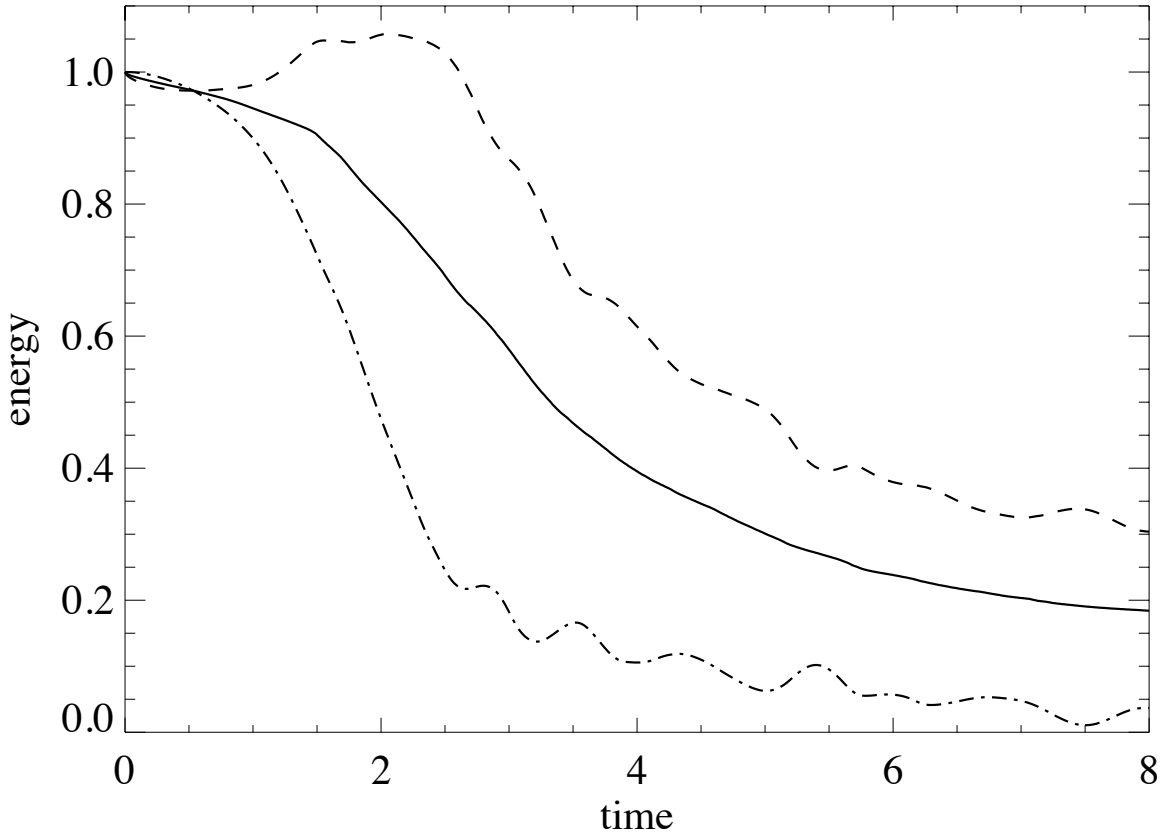

Fig.11 Chen et al.

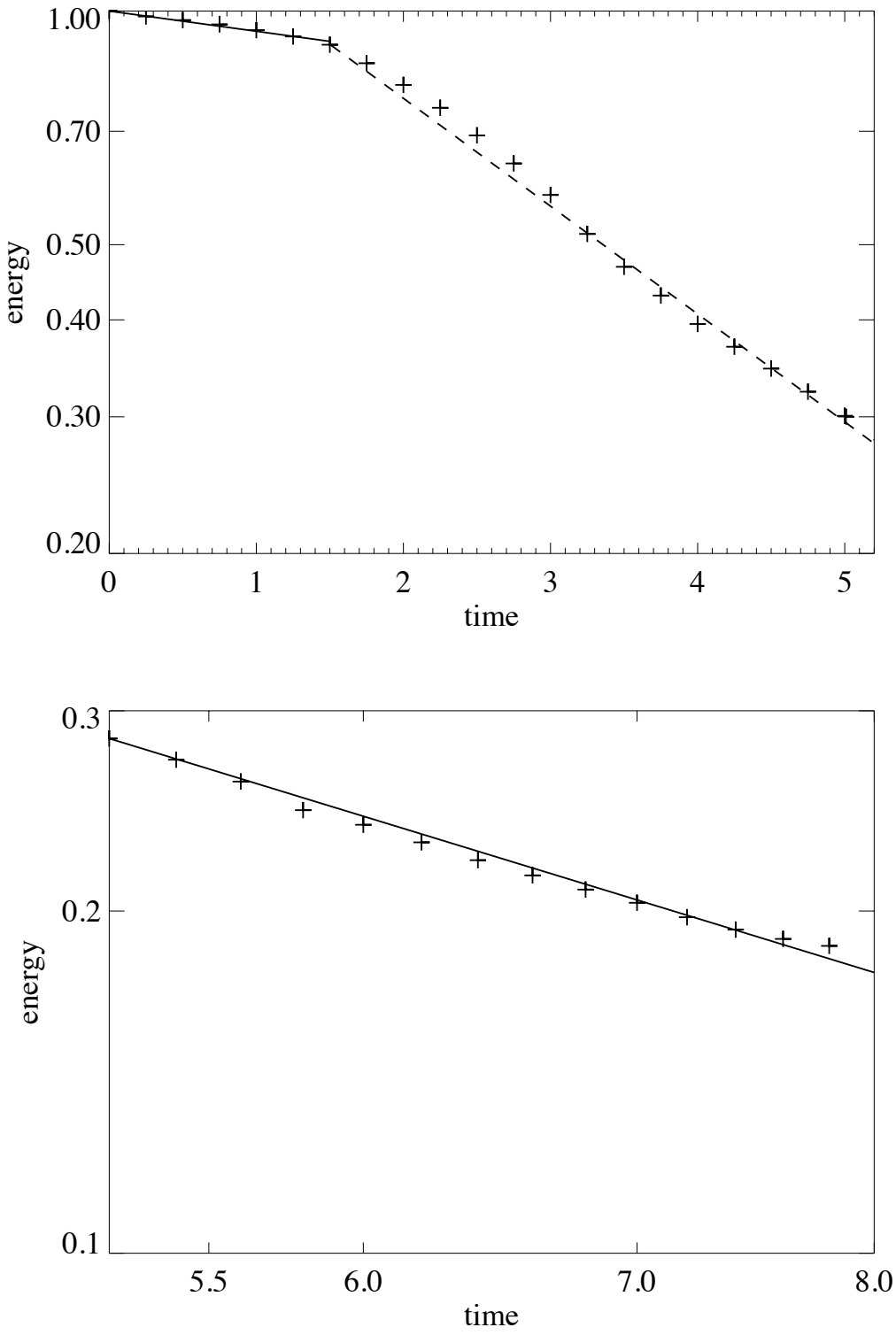

Fig.12 Chen et al.

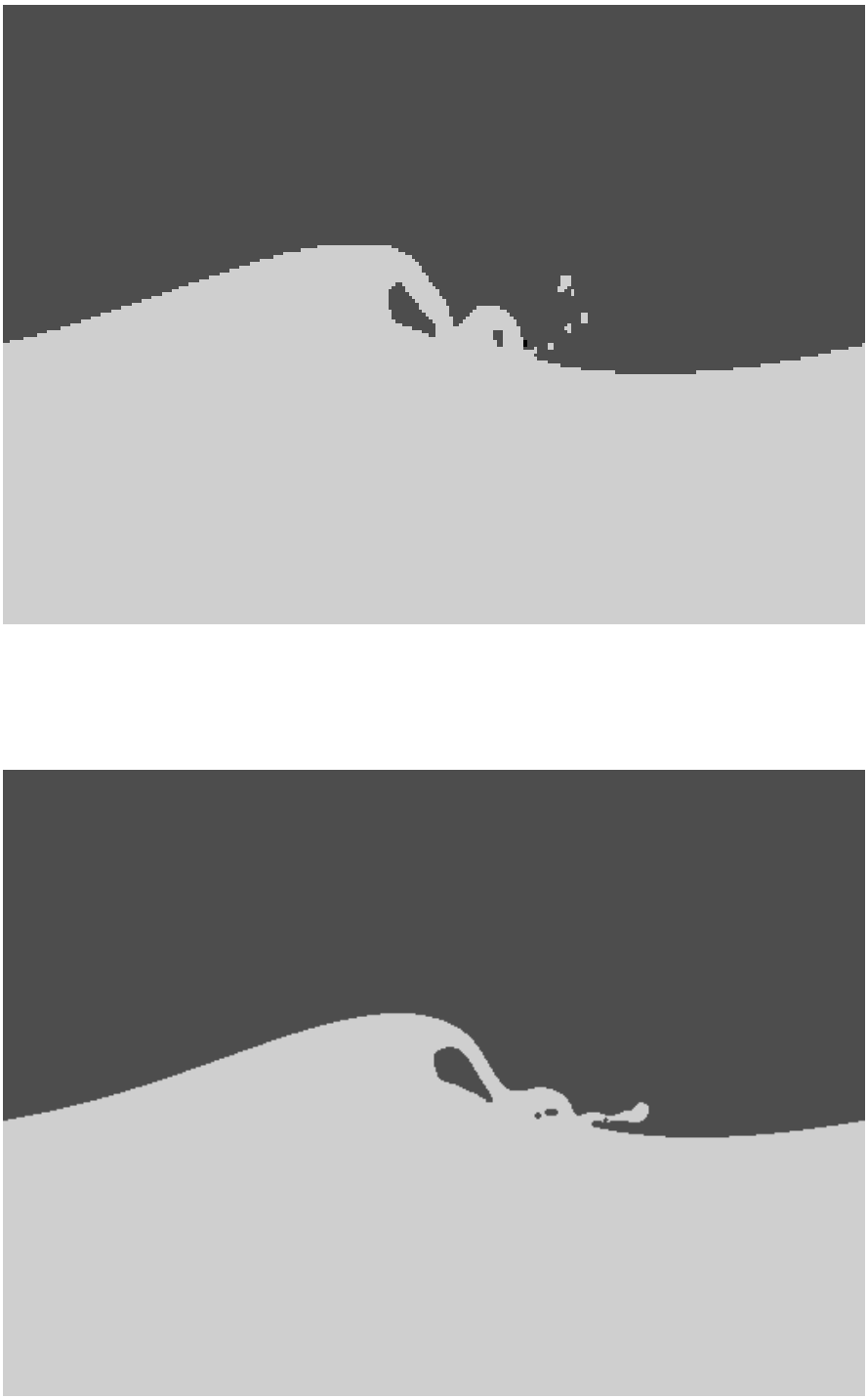

Fig.13 Chen et al.

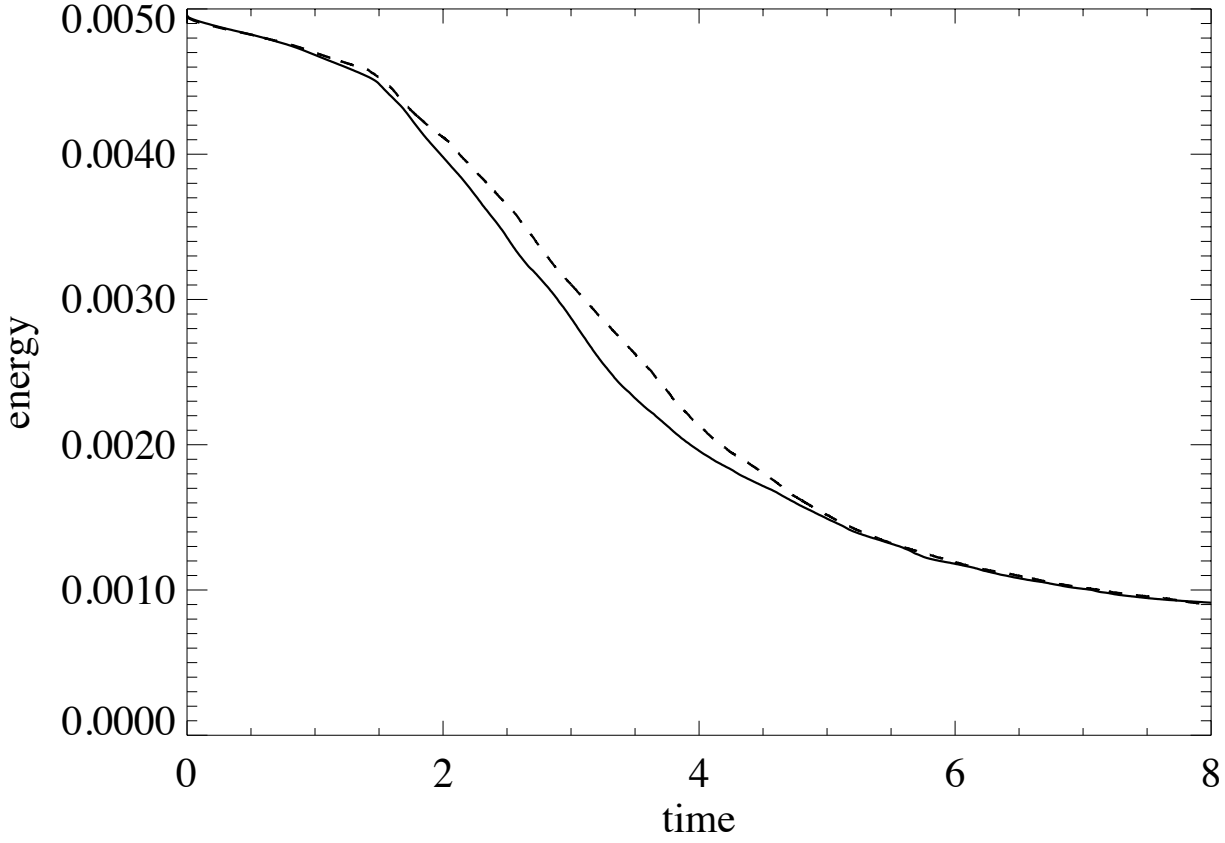

Fig.14 Chen et al.